# High-temperature reactive synthesis of the Zr-Ta multiboride with a supercomposite structure

| | |
|---|---|
| Journal: | *Journal of the American Ceramic Society* |
| Manuscript ID | JACERS-49126.R2 |
| Manuscript Type: | Research Article |
| Date Submitted by the Author: | n/a |
| Complete List of Authors: | Demirskyi, Dmytro; Tohoku Daigaku Zairyo Kagaku Koto Kenkyujo,<br>Suzuki, Tohru; National Institute for Materials Science, Research Center for Functional Materials<br>Yoshimi, Kyosuke; Tohoku University, Department of Materials Science and Engineering<br>VASYLKIV, Oleg; National Institute for Materials Science, Research Center for Functional Materials; |
| Keywords: | composites, borides, hardness, strength |
| Author-supplied Keyword: If there is one additional keyword you would like to include that was not on the list, please add it below:: | supercomposite architecture |
| | |
| Note: The following files were submitted by the author for peer review, but cannot be converted to PDF. You must view these files (e.g. movies) online. | |
| SVideo1.mp4<br>SVideo2.mp4<br>SVideo3.mp4<br>SVideo4.mp4 | |

# High-temperature reactive synthesis of the Zr-Ta multiboride with a supercomposite structure

D. Demirskyi (a,b,c)†, T.S. Suzuki(b), K. Yoshimi (c), O. Vasylkiv (b)†.

(a) WPI-Advanced Institute for Materials Research (WPI-AIMR), Tohoku University, 2-1-1 Katahira, Aoba-ku, Sendai, 980-8577 Japan

(b) National Institute for Materials Science, 1-2-1 Sengen, Tsukuba, Ibaraki 305-0047, Japan

(c) Department of Materials Science and Engineering, Tohoku University, 6-6-02 Aramaki Aza Aoba, Sendai, 980-8579, Japan

This study reports the formation of a ceramic composite consisting only of boride phases with an artificially created hierarchical superstructure. Such a composite was formed during the reaction-driven consolidation process using a mixture of $ZrB_2$, tantalum and amorphous boron powders. The homogeneity of the reaction between these powders at 1900 °C allowed the forming of a highly reproducible and repetitive superstructure where $Ta_3B_4$ forms a chain-like mesh which entraps the $ZrB_2$, ZrB, TaB and $(Zr,Ta)B_2$ phases. The multiboride ceramic composite exhibited extremely high hardness: 28.6±3.2 GPa or 22.6±0.6 GPa. These were estimated using 98 N and 196 N loads, respectively. At 2000 °C, the multiboride composite showed a strength of nearly 400 MPa and fractured in an elastic manner at the loading rate of 2.5 mm/min. This level of strength is usually observed for the bulk zirconium diboride at room temperature. The main factors leading to the improvement of the mechanical properties were considered to be the formation of the $(Zr,Ta)B_2$ solid solution as well the composite structure.

## 1. Introduction

It is well established that the borides of transition metals, such as $TiB_2$, $TaB_2$ and $ZrB_2$, are being widely used for a variety of application including thermal protection systems, cutting tools, etc.

† Authors to whom correspondence should be addressed, Dmytro Demirskyi, demirskyi.dmytro.e2@tohoku.ac.jp, Oleg Vasylkiv oleg.vasylkiv@nims.go.jp

[1]. Due to the recent interest in ultra-high-temperature ceramics (UHTCs) capable of withstanding high-temperatures and high external loads in severe or extreme environments, the number of publications about the zirconium diboride is particularly high [2].

However, the processing of the monolithic $ZrB_2$ is not an easy task. First, zirconium diboride requires a relatively high consolidation temperature due to the presence of metal-covalent, covalent-ionic bonds in the diboride crystal cell [1,2]. Second, the raw powder may have a surface oxide layer, which [2,3] if not removed, will slow down the densification, or will result in the formation of a considerable amount of the oxide [3]. Finally, the strength at elevated temperature was extensively studied, but still requires improvement [2,4,5]. The solid-solution diborides have received considerable attention [6–10] in order to improve their strength. Diborides are not the only borides for transition metals, as other compounds such as monoborides, $Me_3B_4$ or dodecaborides, were also reported [1,11–14]. Some of these borides are considered to possess a 'superhardness' based on the first-principles calculations or machine learning [15–20]. These phases may contribute to the improvement of the mechanical properties if these are present in the composite with the diboride. Although, some of these borides with a melting point approaching 3000 °C [14] are not considered as UHTC compounds mainly due to the lack of the reports on their high-temperature properties.

Considering these observations within the present study, we attempted to create a multiboride composite with a hierarchical superstructure based on $ZrB_2$. Creating such a composite allows one 1) to grain refinement due to creation of an interface between the composite phases; 2) to create a solid-solution between $ZrB_2$ and $TaB_2$ in order to explore if the solid-solution strengthening will improve the strength at elevated temperatures. Finally, 3) to reinforce the composite with other boride phases, such as $Ta_3B_4$ or ZrB, in order to improve the hardness and toughness of the

composite. To fulfill ideas, we applied a reactive sintering approach using $ZrB_2$, Ta and amorphous boron. Spark-plasma sintering served as a reactive consolidation technique [21]. The high-temperature properties of the multiboride ceramic composite were evaluated using the three-point flexural strength method between room temperature and 2000 °C.

## 2. Materials and Methods

### *2.1 Powders and mixing*

Commercially-available $ZrB_2$ (High-Purity Chemicals, Japan), amorphous B (Wako Pure Chemical Industries, Japan), and Ta (Micronmetals, USA) powders were used as the starting materials. Tantalum powder had the size of 2 to 8 μm, with median size ($d_{50}$) of 3.6 μm was determined by scanning electron microscopy (+325 mesh according to the manufacturer). Tantalum powder was produced by gas atomization and a majority of particles had a spherical shape. Zirconium diboride had a mean particle size of 2.1±0.4 μm, while the boron powder consisted of primary crystallites with sizes ranging from 20 nm to 4 μm [22]. The received untreated powders were mixed using a two-step procedure; in the first step, the Ta and boron powders were mixed, then at the end of these steps, they were quasi-granules covered in fine boron and had the light-red color of the amorphous boron [22]. The second step consisted of mixing these quasi-granules with $ZrB_2$. The first and second steps were performed using the Intelli-Mixer RM-2M (ELMI, Latvia) mixer. This procedure excludes using solvents or grinding the materials. The mixing process and partial crushing of the ceramic particles occur due to fast vibrations in the relatively small volume ( 50 ml). As a rule, a higher vibration mode was used during the first step. The Ta+B mixture was prepared using a 1:1.8 molar ratio. The excess in boron was added to account for evaporation of the boron from the powder mixture during the heating to the elevated temperature in the spark-plasma sintering (SPS) process or due to formation of other borides. We

targeted the Ta:B 1:1.33 ratio as for processing at 1900 °C would require at least a 35 mol.% increase in boron in the Ta+B mixture. The 1:1 weight ratio of $ZrB_2$ and Ta+B was used in the second step.

*2.2 SPS processing*

After this mixing, the powders were placed in the SPS graphite die. We used an inner Ta-foil (Sigma-Aldrich Chemie, 0.025 mm thick, 99.9+% metal basis) and outer graphite foil configuration in which the Ta-foil is used to isolate the powder mixture from the graphite felt or the graphite die. Thus the hollow tantalum cylinder was filled with the powder mixture. The top and bottom of such a cylinder were covered with two circular cut-outs made from the tantalum foil. These steps are necessary to minimize the diffusion of carbon [23] into the powder mixture during the SPS process. The SPS experiments were conducted using the 'Dr. Sinter' 1050 (Sumitomo, Japan) unit with a 30-mm die, and typically, 20 to 30 g batches were produced.

The schedule for the specimens prepared in this study had the following major steps: (1) heating to 700 °C in four minutes following (2) a 200 °C/min heating to the densification temperature within 1900 °C. At 1900 °C (3) a dwell of 5 min was used as a homogenizing step (see *section 2.4* and *Suppl. S1* for details). (4) cooling to 1800 °C using a rate of 20 °C/min was then performed, followed by (5) a decrease in temperature to 1400 °C with a rate of 40 °C/min. At 1400°C, a (6) 20-min dwell was used. The final step included cooling to 600 °C in 40 minutes (i.e., 20 °C/min). The pressure of 45 MPa was maintained during the heating, consolidation and cooling stages. Argon gas at the flow rate of 2 L/min was used.

*2.3 Characterization*

An X-ray diffraction (XRD) analysis (D8 Advance, Bruker, Karlsruhe, Germany) was performed on the polished surfaces of the bars after the flexural tests using Cu-Kα radiation. The intensity data were collected over the 2θ range of 30°–145° in steps of 0.02° using a sampling time of 10 s for each step. The software used for refinement was TOPAS (TOPAS Ver. 4.2, Bruker AXS, Germany) or Profex [24]. Instrumental broadening was determined using a NIST 660b $LaB_6$ standard run under the same conditions for each sample.

The structural characteristics of the multiboride ceramics were studied by scanning electron microscopy (SEM, JCM-6000, JEOL) with secondary (SE) or backscattered electrons (BSE mode). Energy Dispersive X-ray Spectroscopy (EDS) was performed using a JEOL DX200s unit. We used a 1k resolution and a dwell of 2 μs for acquiring the element maps. For the analysis of the EDS data, we used NIST DTSA-II software [25]. The spectra of the bulk $ZrB_2$, $TaB_2$ and equimolar solid-solution between these diborides made on specially prepared specimens served as a reference point in the analysis of the solid-solutions. In order to verify the presence of oxides, the bulk $ZrO_2$ and $Ta_2O_5$ were also probed. Oxides were prepared using powders from Wako Pure Chemical Industries, Japan.

The three-point flexural strength was determined using rectangular blocks (1.5×2×25 mm, ASTM C1211−13, configuration A) and the strength testing equipment that was previously described in detail [26]. The high-temperature tests were performed in argon. The temperature inside the hot zone was controlled by two thermocouples and an IR pyrometer. The pyrometer was used to control the temperature above 1800 °C. The vacuum was pumped to $4 \cdot 10^{-3}$ Pa and backfilled with high-purity argon at least 3 times for the high-temperature tests. Argon had a purity of 5.0 (i.e. 99,999% purity). A span of 16 mm was used. If not stated otherwise, measurements were performed with a loading speed of 0.5 mm/min.

The fracture toughness of the ceramics was evaluated by the specimen bending testing which contained a single edge through-thickness notch following ASTM C1421–10 (single edge through-thickness notch 3 mm×4 mm×25 mm, notch width 90 μm, depth 0.4–0.6 mm, a/W <0.15). The toughness was tested in the same direction as the pressure was applied during the SPS consolidation. Details of the testing configuration and the notch profile were presented in ref. [27]. Two measurements were performed at the loading speed of 0.5 mm/min. The flexural strength data were averaged based on at least three tests at the elevated temperature and by seven tests at room temperature. Alternatively, the indentation fracture toughness was calculated using the half length of the crack $c$ formed around the corners of indentations at the load $P$ of 196 N using the following equation [28]: $K_{IC} = 0.0725\ (P/c^{3/2})$.

The hardness was determined by a Vickers hardness tester (Akashi, AVK-A, Japan) using loads of 98 N and 196 N with a dwell time of 15 s following the standard procedure (ASTM C 1327–15).

*2.4 Criteria for selection of final processing parameters*

In order to obtain a ceramic with strength and hardness higher than for bulk $ZrB_2$ [2,4] we performed a number of the SPS trials using a factorial design with additional center point [29]. After completing 15 SPS runs (see *Suppl S1*) specimens were checked for three criteria: (1) presence of cracks; (2) hardness of the composite and (3) flexural strength at room temperature. For the two latter parameters we evaluated a response surface based on the initial data [29]. **Figure 1** shows the contours for the linear regression performed using strength and hardness data.

The strength used for the construction of the response surface was measured using one bar per different SPS conditions. The hardness was evaluated using a load of 196 N and diagonal was checked after the testing using the optical viewer of the hardness tester. The response surface had

a shape of the 'rising ridge' and the peak in the strength or hardness can be expected using higher dwell time at 1400 °C. Nevertheless, the SPS runs #8 and #12 (see *Suppl. 1*) were fairly cracked, hence it, it was decided to use a 20/5 configuration for the consolidation. One can presume that dwell at 1400 °C controls partial relief of the micro-stresses formed during cooling from 1900 °C. Hence, it is expected, that elastic anisotropy is mainly responsible for the introduction of micro-stresses and microcracks due to the different isotropy in the elastic constants for the phases of the composite (*see Suppl 2*).

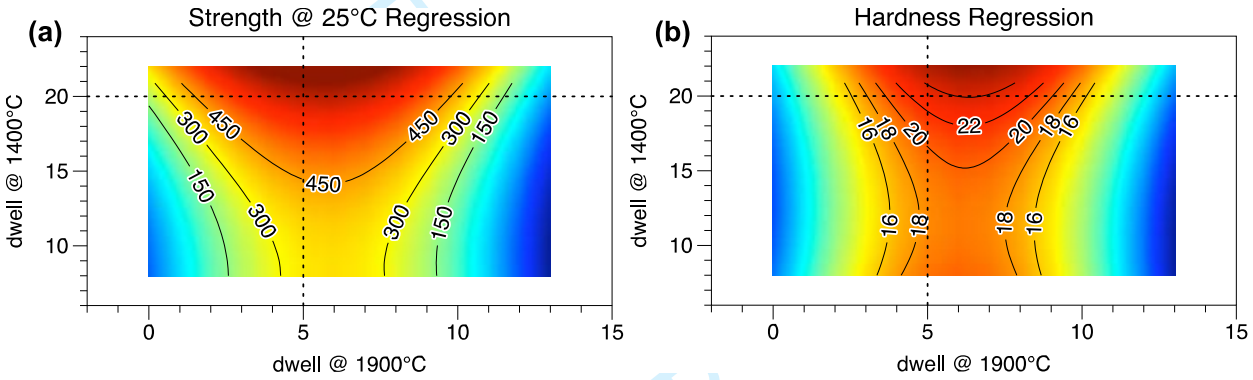


**Figure 1**. Response surface representation of the (a) room temperature flexural strength and (b) hardness using the two-step SPS processing. The x-axis is the dwell being used for consolidation, while the y-axis is the dwell at 1400°C that is being used at the cooling stage in order to control strain induced by the difference in the coefficient of the thermal expansion of boride phases. Dotted lines show the 20/5 configuration used for the preparation of the multiboride ceramic composite used for the high-temperature flexural tests. Hardness was evaluated using a 196 N load. The strength was evaluated using a three-point flexural test.

## 3. Results and Discussion

### *3.1. Composite architecture*

After the spark plasma sintering at 1900 °C, the ceramic had a distinctive microstructure (**Fig. 2**), which can be easily described as a supercomposite due to the fairly high reproducibility of the structural elements. (see *Suppl. S3* for image from an optical microscope). This composite features ~20–100 μm $ZrB_2$ grains that were entrapped in the binary solid solutions, such as $(Zr,Ta)B_2$ and $(Ta,Zr)B_2$, and the contribution of Zr to these solid solutions varied from 72–79 to 34–42 mol.%, respectively. At the same time, these quasi-cells were entrapped with a quasi-continuous chain-like layer of the $Ta_3B_4$. At the border of these cell-chain composites ZrB and TaB were seldomly observed, the TaB served as a layer with a thickness below 5 μm for the $Ta_3B_4$ phase clusters. In addition to these phases, the whole composite was interpenetrated by the thin thread-like ZrB or $ZrB_2$ phase, which remains unaffected by the reaction between $ZrB_2$ and Ta. As such, $Ta_3B_4$ and two binary $(Zr,Ta)B_2$ solid-solutions act as a composite matrix, whereas the fine $ZrB/ZrB_2$ quasi-continuous fibrils act as a reinforcing phase.

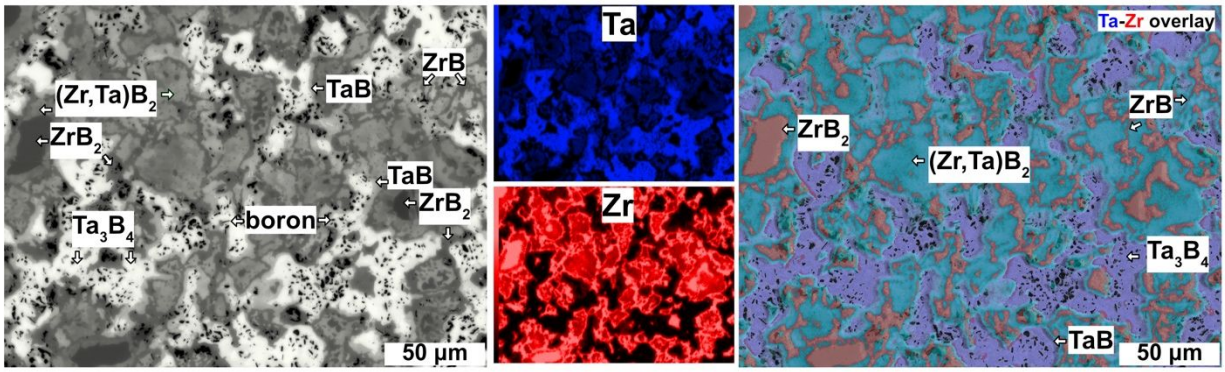


**Figure 2**. Representative microstructure of the multiboride ceramic after consolidation at 1900 °C. Black areas are unreacted boron and pores. Right image shows an overlay of Ta (blue) and Zr (red) maps after the EDS.

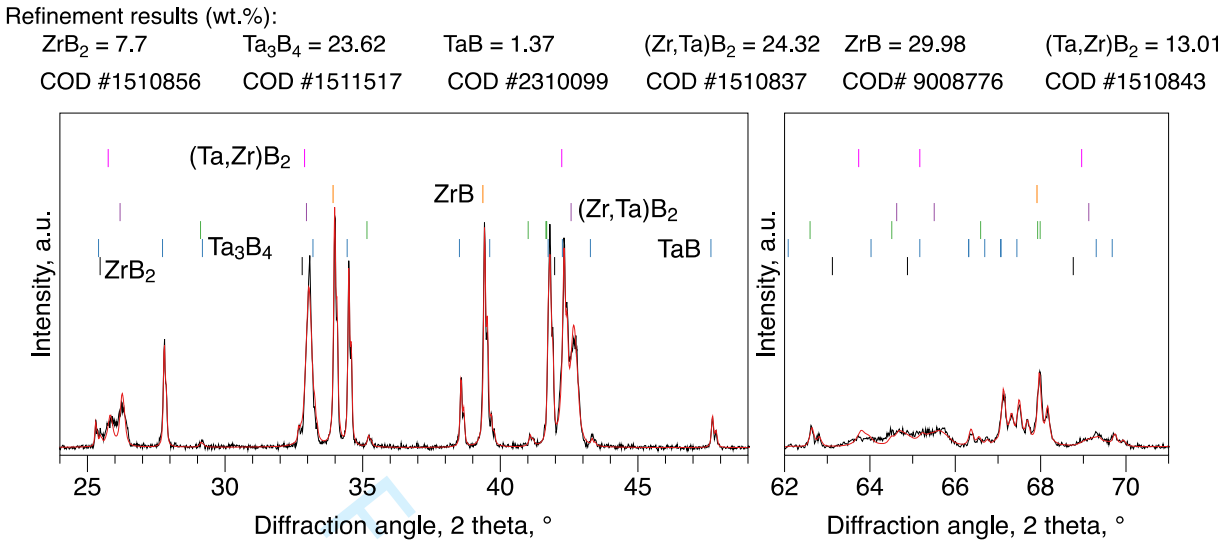


**Figure 3**. X-ray diffraction pattern observed after the SPS consolidation. Vertical lines indicate the Bragg position for the boride phases. Red solid line shows the refinement performed using the Rietveld method. ($\chi^2$ – 2.06, GoF – 1.44). Initial structures used during the refinement process can be obtained using the Crystallography Open Database (COD) number.

SEM also confirmed the presence of fine pores (~0.2 vol.%) and a boron phase (up to 3 vol.%). The boron was not detected by the X-ray diffraction analysis (**Fig. 3**), but it was usually located in the (Zr,Ta)$B_2$ solid solution or $Ta_3B_4$. Hence, it would be safe to assume that these boron grains seldomly observed with the plate-like shape were the crystalized grains of the unreacted amorphous boron presumably entrapped during the cooling process. **Table 1** summarizes the main features of the phases identified for the multiboride ceramic composite [14,30–42].

The Rietveld refinement performed on the SPSed composite suggested that the main phases were two diboride solid solutions of 35 wt. % (lattice parameters (i) $a$ = 3.133 Å, $c$ = 3.399 Å (42 mol% Ta); and (ii) $a$ = 3.142 Å, $c$ = 3.456 Å (60 mol.% Ta)), cubic zirconium boride ($a$ = 4.573 Å, 30 wt.%) and $Ta_3B_4$ (23 wt.%). EDS indicated that the ZrB/TaB had a 52:48 mol.% ratio between the

metal and boron, and these can be easily distinguished from the $ZrB_2$ or $(Zr,Ta)B_2$ solid solutions. Neither the EDS probes indicated the presence of the tantalum diboride. The zirconium diboride phase was highly strained. One can presume that the strain imposed on this phase by the surrounding solid-solutions [43] was compressive. The X-ray density was determined to be 8.473 g/cm$^3$, while the bulk density measured by the water-displacement method was 8.67 g/cm$^3$. The difference between the two values was assumed to be due to the Ta to Zr values in the diboride solid solutions as the X-ray density does not account for the homogeneity range observed by the EDS probing.

Cubic zirconium boride was observed in refs. [44–47]. It was noted that it has a rock-salt like structure as does zirconium carbide. Unlike the carbide or nitride [48], the homogeneity range for this boride is quite low. For ZrC, the lattice parameter will depend on the C deficiency within the range of 4.65 Å to 4.71 Å[30], while for the zirconium nitride, the lattice parameter should lie between 4.579 Å to 4.573 Å [48]. For zirconium monoboride, the range of the lattice parameters was reported to be 4.65 Å to 4.68 Å in ref. [45] and 4.64(7) Å in ref. [46]. The lattice parameter of cubic zirconium boride determined in the present study was $a = 4.573$ Å, which is in general agreement with the previous results. Note that the ZrB is an intermediate phase and it was most likely formed during the cooling process, hence one may expect that the local deficiency in boron may influence the lattice parameter. Similar observation was made for the $ZrB_2$–W system in ref. [47].

*3.2. Reaction route and boride phase specifics*

Glaser [44] reported that the ZrB was formed using hot-pressing at 1100 °C, hence the formation of this intermediate phase is believed to be when all the initial $ZrB_2$, Ta and B powders were in the

system. Alternatively, ZrB can be formed during the cooling process, which seems more likely as this phase was found to have the form of needles and in a majority of the cases, filled the gap between other the phases. This significantly reduced the porosity and allowed this phase to interpenetrate through the composite (see **Figs. 2,4**). At the same time, Glaser [44] noted that a phase like, $ZrB_{12}$ or ZrB, will not be formed in the excess of boron if the carbon is present in the system. Brewer and Haraldsen [49] confirmed this observation but added that ZrB or TaB is unstable in the presence of the graphite. We used the Ta-foil to minimize the carbon diffusion during the SPS, however, we can hypothesize that some carbon was present in the raw zirconium diboride as it was previously reported for other diborides [50]. Minor carbon presence (C <0.25 wt%) was within the specification provided by the manufacturer. The total carbon contents were analyzed using CS-800 (Eltra GmbH, Haan, Germany).

The large grains of the $ZrB_2$ were seldom found up to 1 mol.% of C. The tantalum and zirconium monoborides were detected by the EDS and XRD. These results indicated the possibility of only the negligible presence of carbon in the system. Formation of the $Ta_3B_4$ over the $TaB_2$ seems to be attributed to the loss of the metal to the $(Zr,Ta)B_2$ solid solutions, while the boron was directly reacting with the Ta forming a layer of TaB covering the $Ta_3B_4$ grains. Another issue was the loss of boron during heating to 1900 °C. For instance, a separate batch of the Ta+B mixture heated to 1700 °C resulted in a monolithic $TaB_2$ ($a$ = 3.067 Å, $c$ = 3.284 Å). However, the same experiment conducted above 1900 °C will always result in the appearance of the $Ta_3B_4$ or TaB.

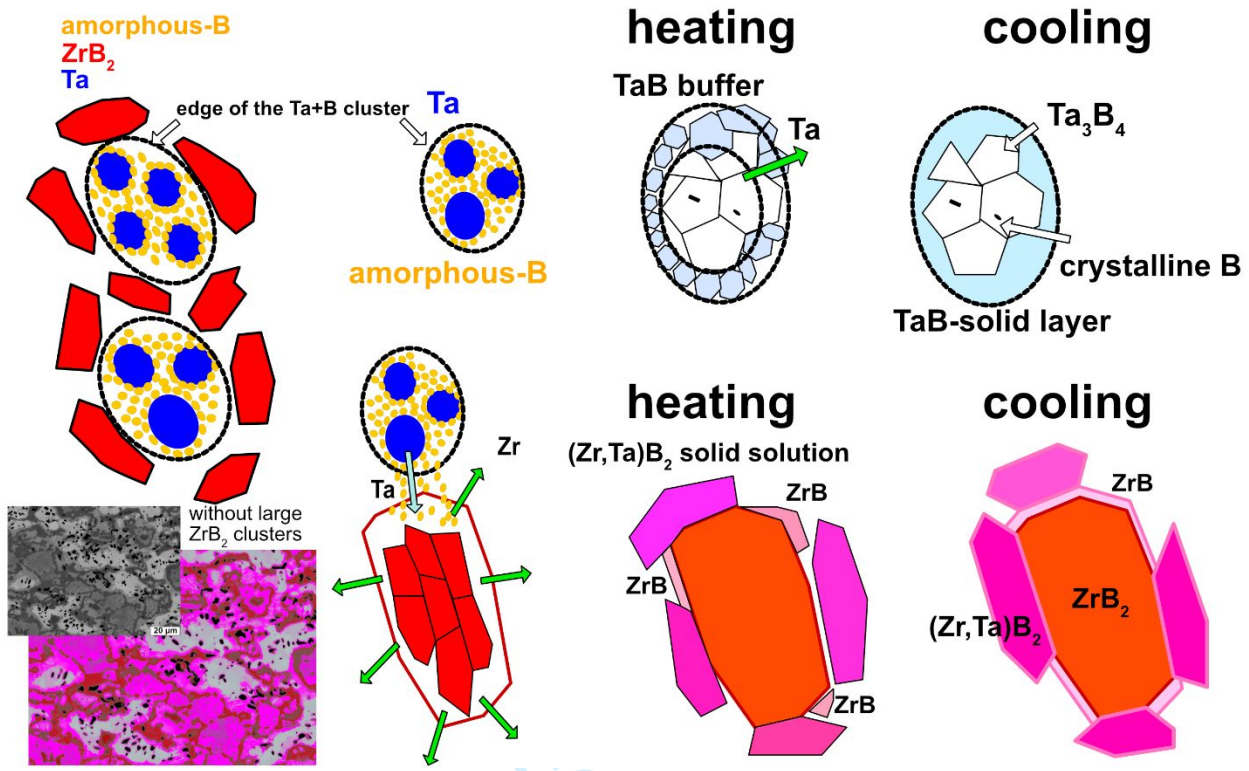


**Figure 4**. Schematic formation of the phases during the reaction and cooling stages of the consolidation process. Note that the Ta-B mixture was prepared, then the $ZrB_2$ was added the mixture. The inset shows the area where the TaZrB phase is being formed, while the main phase is the diboride solid-solution. Such a scenario is only possible in the ideal mixing case.

In the case of the Zr-Ta-multiboride ceramic, the crystalline boron was present as an entrapped phase inside the $Ta_3B_4$ clusters suggesting that the outward diffusion of tantalum leads directly to the formation of the tantalum monoboride. According to Glaser [44], TaB or $Ta_3B_4$ would be more stable than $TaB_2$ at 2900 °C, however such a temperature was not trialed during the SPS, but it is possible to have a local temperature gradient during the SPS which may lead to this temperature range [51,52]. This idea, obviously, is highly hypothetical considering that a relatively fine grain size was observed in the composite. Furthermore, Kiessling reported the formation of TaB, $Ta_3B_4$ at 1800–1900 °C [11], while Dzyadykevych et al. [53] reported the multistage process of the

borating of boron. In such a process where boron oxide and carbon are present, the formation of the tantalum diboride is the final stage, while the prefinal product should include TaB and $Ta_3B_4$. Portnoi et al. [14] suggested that $Ta_3B_4$ is difficult to produce by synthesis from the elements at temperatures below 1750 °C, hence a complex reaction involving TaB and boron can be expected. Considering these facts, it is more reasonable to interpret the phase formation in the system as depicted in **Fig. 3**. The homogeneity of the mixing procedure might play a predominant role in the formation of the local structure; if fairly large clusters (50 μm) are being formed during the mixing process, it is highly likely that the ZrB/TaB will be formed as an interlayer between the $ZrB_2$ or Ta-B clusters. For the former, the outward Zr diffusion is the more likely scenario during the atom exchange, while for the latter, the Ta should and will tend to escape from the original cluster of Ta+B formed during the mixing procedure.

The $Ta_3B_4$ clusters above 10 μm in size will most likely have an entrapped crystallized boron which will self-assemble, in some instances, into the short-rod grains. The TaB may serve as a porous interlayer during the high-temperature range, but similar to ZrB it will form a dense ~2–5 μm layer covering the $Ta_3B_4$-boron clusters. In the ideal case where there was a uniform contact between the Ta+B clusters and $ZrB_2$ powders (see inset in **Fig. 4**), only the ZrB-TaB solid solution phase will exist, while the fine spaghetti-like $ZrB_2$ or ZrB grains will act as a reinforcing phase. The thickness for these grains is comparable to 4–5 μm (powder $ZrB_2$ had a size of ~ 2 μm). Such a structure can be easily reproduced using 10-mm specimens, however, it was only rarely observed using the 30-mm die and specimen thickness of 6 mm.

### *3.3. Mechanical properties*

#### *3.3.1 Evaluation of hardness and toughness*

The formation of a multiboride supercomposite ceramic resulted in the extremely high hardness (22.6±0.6 GPa using a load 196 N). The indentations using a load of 98 N resulted in a hardness exceeding 30 GPa (**Figure 5**) [35,54–56] which is higher than hardness of $ZrB_2$ [2,35,54–58]. The hardness of $Ta_3B_4$ was reported at the load of 0.49 N (32.8 GPa and 24.0 GPa) [14,58], and for the high-entropy boride $Me_3B_4$, the hardness was evaluated as 25.5 GPa at 9.8 N load [59]. Okada et al. reported that the hardness of TaB, $Ta_3B_4$, and $TaB_2$ single-crystals was 22.8 GPa, 24.8 GPa and 27.2–29.0 GPa, respectively. These were estimated using 0.98 N and 1.96 N loads [12]. Itoh et al. [60] reported the hardness of tantalum monoboride as 22 GPa using a load of 1.96 N.

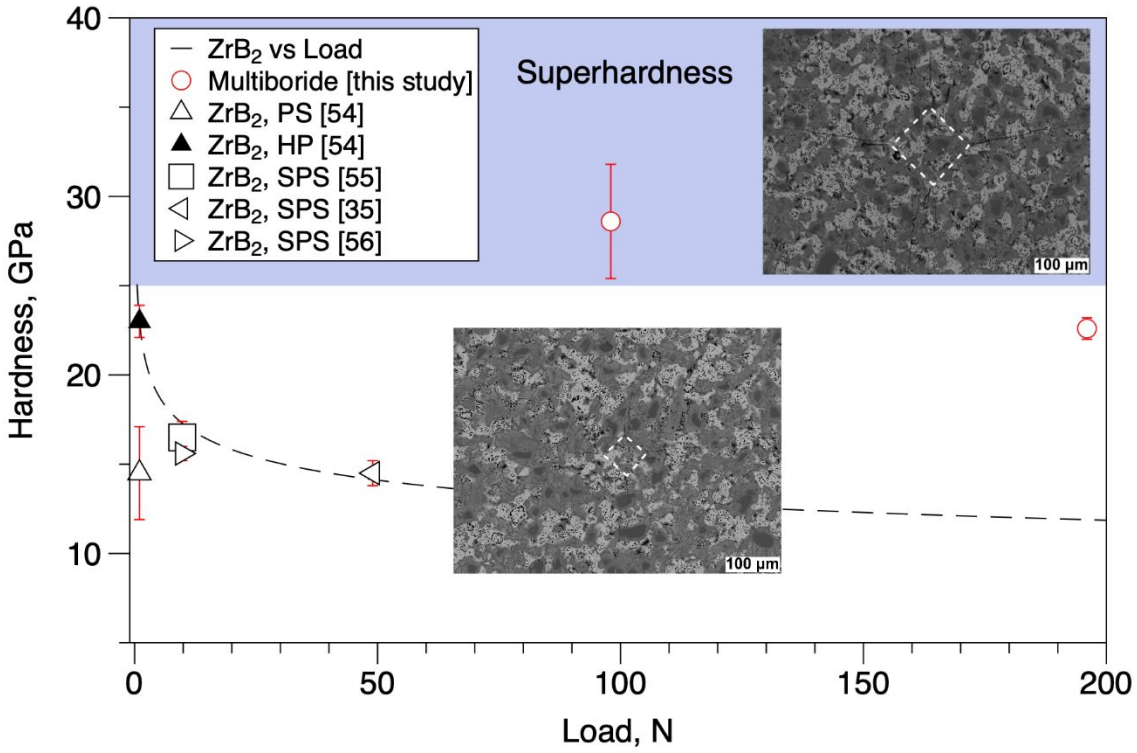


**Figure 5**. The hardness of multiboride and $ZrB_2$ [35,54–56] as a function of load*. Insets illustrate the multiboride samples indented with loads of 98 N and 196 N.

*PS – pressureless sintering; HP – hot pressing; SPS – spark plasma sintering.

Monolithic superhard materials have shown a large load-dependent hardness [61], commonly referred to as the "indentation size effect". This effect for the $ZrB_2$ is illustrated by a dashed line in **Fig. 5**. In the case of a composite with more than two phases such a behavior is possible, but is highly unlikely when using a load exceeding 98 N. Thus, it highly reasonable to assume that an increase in the hardness for the multiboride Ta-Zr ceramic is due to the continuous $Ta_3B_4$ phase or due to the solid-solutions formed between the zirconium and tantalum diborides.

The toughness evaluated by the indentation approach [28] was 4.6±0.4 MPa $m^{1/2}$ (*see Suppl. S4 for details*), which is slightly higher than that expected for the bulk $ZrB_2$ [2]. One can expect that the increase in toughness is due to micro-stresses formed at the interface between the various borides as they have different crystal structure (**Table 1**). The direction dependency of elastic properties is commonly known as elastic anisotropy is mainly responsible for the introduction of micro-cracks and a different isotropy in the elastic constants (*see Suppl 2*). An additional increase in toughness is due to the composite architecture. We can only hypothesize that the continuous nature of the chain-like $Ta_3B_4$ phase will assist in the crack arrest as the toughness using the flexure approach showed an average value of 4.7 MPa $m^{1/2}$ at room temperature, while the high-temperature tests are yet to be conducted.

### *3.3.2 Evaluation of flexural strength and fracture peculiarities*

The room-temperature strength was within 450 and 540 MPa with the median value for the seven tests of 505 MPa. This is higher than that for the bulk zirconium diboride of 381±41 MPa [4], but is in the agreement with the fine-grained tantalum diboride of 500±20 MPa [23]. With an increase in the temperature, the multiboride ceramic showed a clear peak in strength at 1000 °C followed by a decrease in the strength up to 2000 °C (see **Table 2**)[4,7]. Only linear strain-stress curves

were observed below 2000 °C, while at 2000 °C at the rate of 0.5 mm/min composite exhibited a considerable plasticity. This allowed the specimen to withstand a very high stress without any fracture. A closer examination of a typical bar from such a test is presented in **Fig. 6**. Clearly the crack was formed during the flexural test, but it does not seem to propagate inside the specimen and is only limited to the surface-near area (the maximum visible crack extension was below 200 μm). This observation suggests that there is a phase in the composite which not only contributes to the macroscopic plastic deformation, but also limits the crack propagation by, presumably, a microplastic field in the front of the crack propagation [6,62,63].

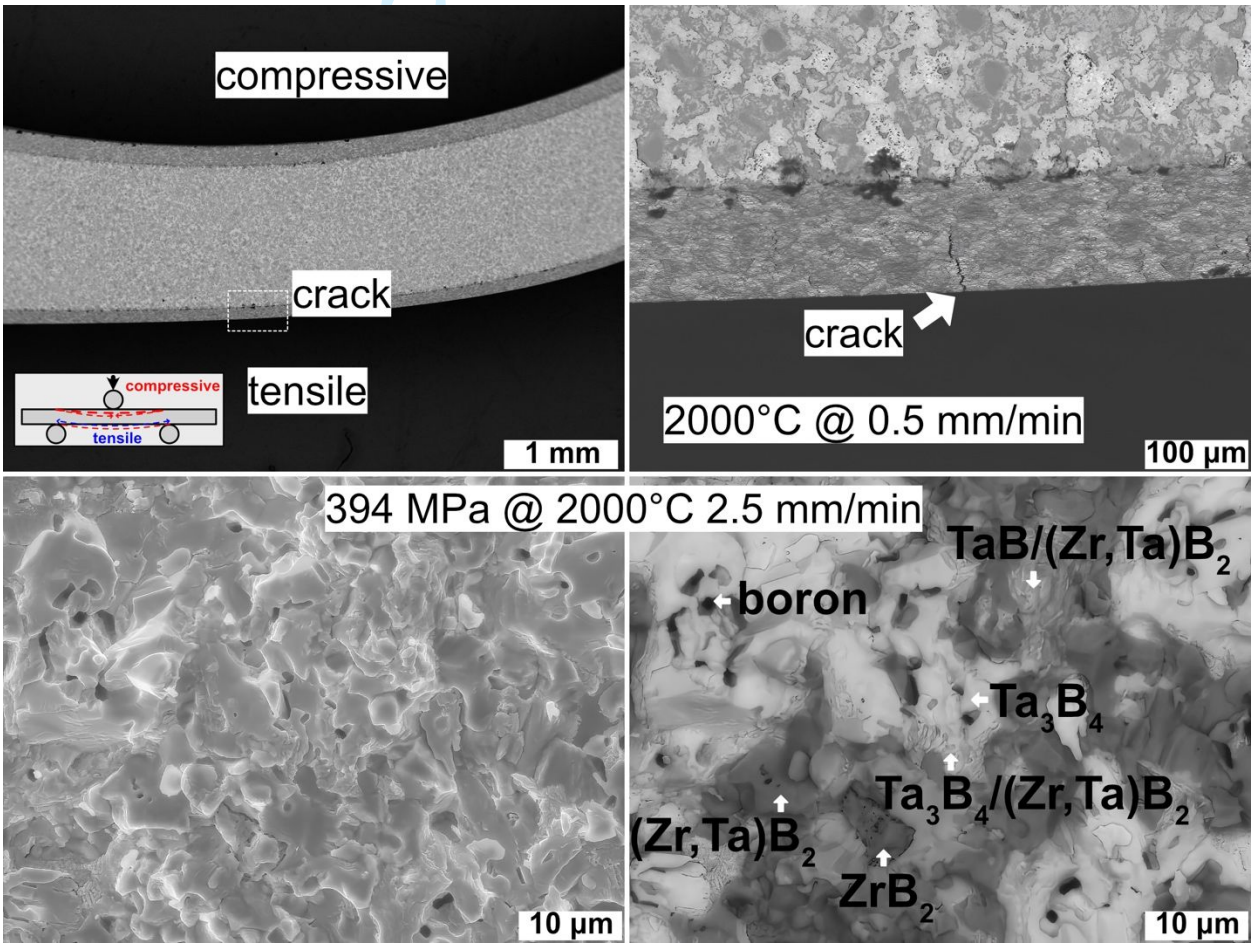


**Figure 6**. Macroscopic fracture details on the flexure of the multiboride ceramic composite at 2000 °C using a 0.5 mm/min loading rate. Representative fracture at 2000 °C using a 2.5 mm/min

loading rate using SE and BSE images. Inset shows the loading procedure during the three-point flexural strength test.

With an increase in the loading rate up to 2.5 mm/min, it was possible to achieve fracture of the specimen. The fracture analysis suggests that the majority of the phases still predominantly underwent a intergranular fracture, which is not typical for bulk diborides at these temperatures [5], and may explain the relatively high strength at elevated temperatures.

Another observation was the presence of fine-grained particles on the fracture surface of the ceramic (**Fig. 6**). It was initially considered that the appearance of these grains is due to the surface oxidation after the test, but EDS probing suggested that the oxygen content of these grains was significantly below 1 mol.%, which is consistent with the values for that absorbed at room temperature or for the polished specimens. Furthermore, the boron grains showed oxygen below 1 mol.% using the EDS, and the authors presume that this would be the first phase to oxidize in the presence of the residual oxygen. Fracture at 1800 °C (**Figure 7**) revealed the presence of fine $Ta_3B_4$, ZrB and $ZrB_2$ fibrils.

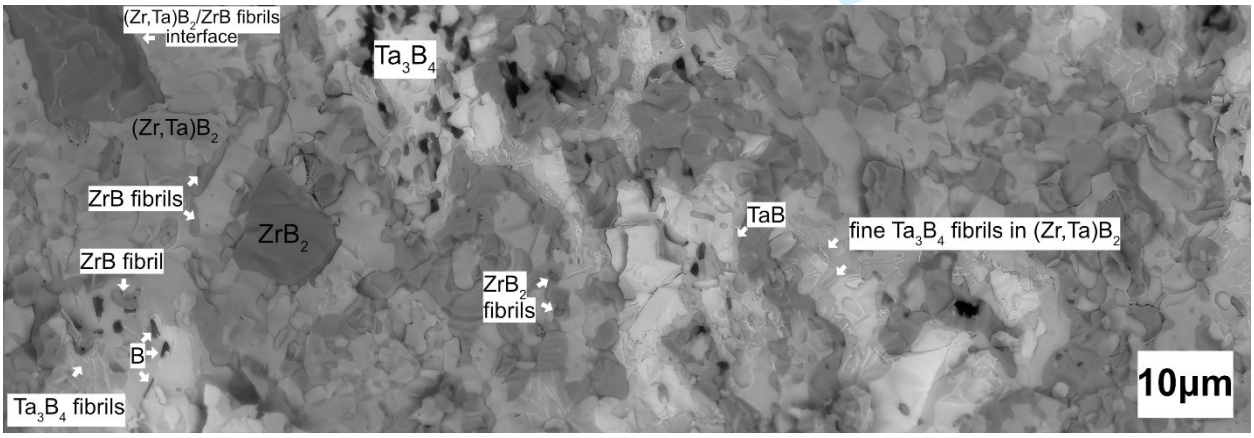


**Figure 7**. Representative fracture of the multiboride ceramics during the flexure at 1800 °C.

Hence, one can speculate that the appearance of these structures is due to the plasticity between the borides at 2000 °C. There were some quasi-lamella sub-grains mainly at the interface of the $Ta_3B_4$ phase, while the observation of the backscattered electrons allows one to see a local gradient in the composition. A similar fracture surface has been observed for the $TiB_2/NbB_2$ double diboride composite, as the formation of a fine subgrain fracture or formation of the needle-like fracture for the $NbB_2$ [6]. Some of these needle-shaped grains appeared at 1200°C in ref. [6], coinciding with the strength increase. Within this study, the presence of these structures was not noted below 1800 °C. Another observation made in ref. [6] is that the $TiB_2$ grains entrapped in the $NbB_2$ matrix showed no visible deformation at 1800 °C, which is similar to the $ZrB_2$ entrapped in the boride supercomposite.

Alternatively, the formation of the needle-like structure is due to deformation or sliding at the $Ta_3B_4$/TaB interface at high temperatures. Although this compound has the melting temperature of 3030±35 °C [14], the $Ta_3B_4$ belongs to the orthorhombic dipyramidal class crystals, which is known for the lamella-like growth habit [38,64]. It is most likely that following a hot-zone exposure after the fracture process, the crystal surface will reassemble into the growth patterns due to the surface diffusion assisted by the argon flow. Okada et al. [12] showed that the $Ta_3B_4$ single-crystals would have a trapezoidal form with the distinctive {010} faces. However, for the TaB Okada et al. [13] reported the formation of the well-developed {010} and {100} faces. In the case of the boride supercomposite, fine TaB inclusions in the $Ta_3B_4$, or $Ta_3B_4$ in $(Zr,Ta)B_2$ were observed for the polished specimens, as seen in **Figure 2**, but these become a regular feature of fracture, especially at 2000 °C.

The fracture of the zirconium diboride grains was rather smooth and had occasional visible slip lines even after the room temperature tests (**Fig. 8**). After the consolidation, this phase is highly-strained ($\varepsilon_{xrd}$~4 $10^{-4}$ a.u.), while after the elevated temperature tests, it follows the temperature: strain increases at 1000 °C, and is fully relaxed at 1800 °C ($\varepsilon_{xrd}$~1.8 $10^{-4}$ a.u.). These observations suggest that micro-stresses may explain the high strength of the Zr-Ta multiboride ceramics at 1000 °C, while a more complex situation is occurring at 2000 °C.

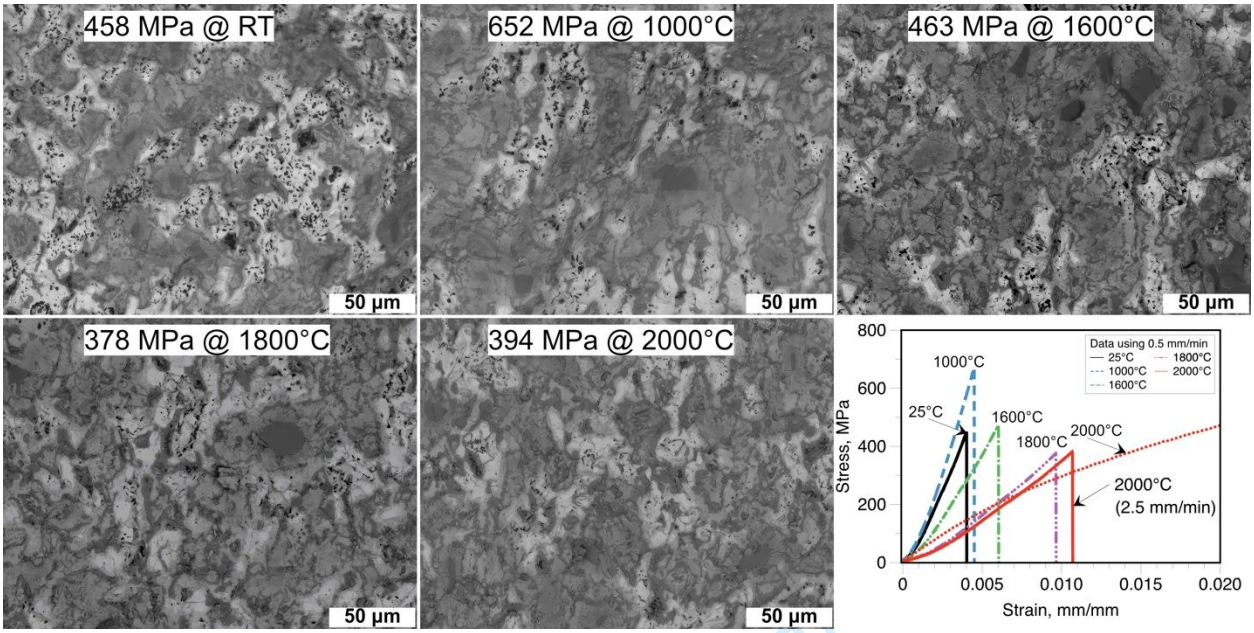


**Figure 8**. Effect of temperature of the flexural test on the fracture behavior of the multiboride ceramic using a loading rate of 0.5 mm/min. The right-bottom image shows the typical shape of the strain-stress curves using loading rate of 0.5 mm/min and 2.5 mm/min at 2000 °C (solid red line).

*3.3.3 Interpretation of the high-temperature fracture at 2000°C*

Previously, the following fracture specifics were observed during the fracture of the diborides: onion-like fracture [7,26] or terrace-like [65,66]. These can be reasonably explained by the surface

diffusion, i.e., grooving [67], or thermal etching by the hot argon gas. Another process [68] occurring on the exposed boride surface is the evaporation of boron which also causes grooving and is a known issue for the $LaB_6$ cathodes [69]. Because the surface is significantly involved and borides will have metal and boron atoms exposed at the surface [68], one may consider this process to be a reverse-one to that of the synthesis for orthorhombic borides as observed by Okada et al. [12,13]. The process for the evolution of the surface during the crystal growth can be visually predicted using CrystalGrower [70]. The crystallographic data were used from refs. [11–13], and the energy used for the calculation was 95 kJ/mol as an activation energy from ref. [71]. Although the activation energy is for the $HfB_2$ hot-pressing, it was concluded in ref. [71] that the controlling diffusion mechanism was either interstitial diffusion or surface or boundary diffusion. In the discussion it was underlined that surface or grain-boundary diffusion should have lower activation energies than the bulk vacancy diffusion. Moreover, the activation energy was determined for the temperature range of 1400–1900 °C, which is consistent with the microstructure evolution under discussion (2000 °C). Leitnaker et al. [72] suggested that the heat of formation of TaB was 160 kJ/mol, while other borides including $TaB_2$ should have heat of formations between 160 kJ/mol and 270 kJ/mol.

The results of the numerical simulation of the growth process for $Ta_3B_4$ are presented in **Fig. 9** (see *Suppl. S5* and *video files* for details). One can see the formation of the step-like or terrace structure, which in the case of the simulation is directly connected to the surface diffusion during the crystal growth. Obviously, the identical process can be expected for $ZrB_2$, $TaB_2$ or any other boride and the only difference will be in the size of the growth-steps (grooving steps) and their crystallographic orientations. Thus the results in refs. [7,26,65,66] for the diborides can also be interpreted as the vaporization of boron.

Another difficultly in interpreting fracture at 2000 °C is due to the fact that fracture at the elevated temperature is directly connected to the crystal structure of the boride. Considering the reports of [1,30,31,48,73,74], a variety of fracture modes in the diborides can be connected with the orientation of the crystal plane in the grain with respect to the plane of the crack propagation as the slip system {1010} <1120> that should be dominant at elevated temperatures, while the {0001} <11-20> is the secondary one (**Figure 9**).

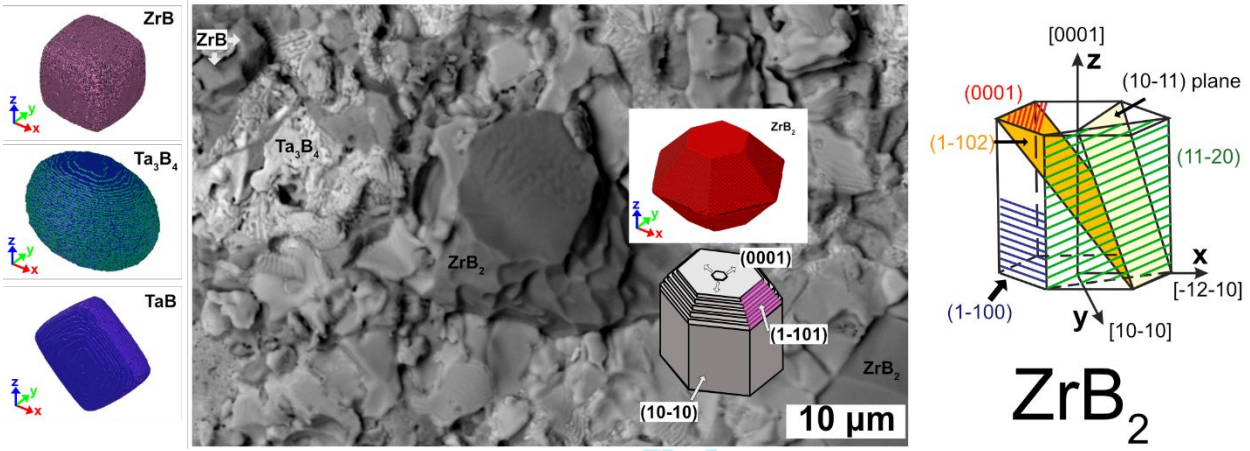


**Figure 9.** Fracture of the multiboride ceramic composite at 2000 °C when a $ZrB_2$ grain has a shape typical of the {0001} plane. Right images and the inset for $ZrB_2$ show formation of the step-like or terrace structure during the surface grooving process for borides at 2000 °C. These images illustrate the formation of the grooving steps (growth steps) during the exposure of the various borides to temperature of 2000 °C. See *Suppl. S5* and *video files* for details.

### *3.3.4 Factors contributing to high-temperature strengthening*

The authors did not find any details about the high-temperature behavior of zirconium/tantalum monoboride or $Ta_3B_4$ during the preparation of this study. The data for the $TaB_2$ are limited to refs. [7,26,27] in which the $TaB_2$ composites were examined. Because the major portion of the

multiboride composite (**Fig. 3**) is the solid-solution phases between the Zr and Ta diborides, it is reasonable to assume that these solid-solutions will control to a certain extent the strength vs temperature behavior. In this study, only 16% of the original $ZrB_2$ remained unreacted, suggesting that the majority of the diboride is being transformed into the solid-solution or ZrB. Considering that the multiboride composite showed a higher strength that is expected for the bulk $ZrB_2$ (**Table 2**), the controlled tantalum doping of the $ZrB_2$ seems to be a reasonable strategy for improving the mechanical performance of the $ZrB_2$-based composites.

Another possibility is to use secondary phases to promote strength. For $ZrB_2$-based ceramics, Zr–Fe–Co–Si, Al-O and Zr-O precipitates were observed in [75]. When the heat-treatment was applied to the $ZrB_2$–SiC ceramic may encourage (i) further reaction with phases at the boundaries and (ii) alter the dislocation density in the $ZrB_2$ or SiC. The latter will affect the mechanical properties such as strength at room-temperature. Silvestoni et al. [76] reported the formation of $ZrO_2$ and W nanoparticles during the flexural tests at 1500–2100 °C. Formation of the oxide in this study was due to the residual oxygen in the testing chamber. While the zirconia was in some instances surrounded by the tungsten nanoparticles. The latter observation may indicate a possibility of the local ductile-phase toughening.

Silivestroni et al. [77] suggested that WB, $WSi_2$ or W-C-O agglomerates were mainly located in the triple-junctions after consolidation. Ding et al. [47] indicated that during the sintering at 2100 °C the (W,Zr)B liquid should assist the densification process, and the ZrB and WB phases were entrapped between $(Zr,W)B_2$ solid-solution grains. Ma et al. [78] reported that W segregation at the GBs of the $ZrB_2$-based composite introduces compressive stress on GBs and provides pinning effect, which might suppress the GB sliding at high temperature.

Finally, the Dai et al. [79] analyzed the segregation of the W in $ZrB_2$ using atoms using the density functional theory based calculations. Their results indicate that W segregates strongly into $ZrB_2$ grain boundaries at elevated temperatures. W segregation strengthens $ZrB_2$ grain boundaries should lead to the increase in strength of $ZrB_2$. Both of these observations confirm results of Ding et al. [47] and Silvestroni et al. [77]. These observations indicate that to control the strength a lengthy heat-treatment is required which is in agreement with results of Neuman et al. [75]. One can hypothesize that boron may promote local ductile phase toughening, as it was reported that monolithic boron will have a plastic strain-stress curve during bending above 1200 °C [34].

Because the composite architecture might considerably contribute to the strength, the contribution of the $Ta_3B_4$ cannot be ignored as $Ta_3B_4$ entraps other boride phases using a mesh-like superstructure. In view of the absence of the experimental data on the high-temperature behavior of the $Ta_3B_4$ phase, it would be of considerable interest to replicate the same supercomposite structures in other boride systems. Next steps in the ongoing research include preparation of the composite in the Ta-Ti-B system, and evaluation of the high-temperature toughness.



**Summary**

Reactive consolidation resulted in the creation of a multiboride ceramic composite with a hierarchical superstructure. The multiboride consisted of $ZrB_2$, (Zr,Ta) solid-solution diborides, tantalum and zirconium monoborides, and $Ta_3B_4$. The latter phase formed a macroscopic quasi-chain structure and served as a secondary matrix. The main ceramic was the solid-solution of zirconium and tantalum diboride which is thought to improve the flexural strength up to 2000 °C when compared to the bulk $ZrB_2$ data. The formation route leading to the superstructure formation and composite architecture were discussed. The composite showed a higher hardness than

expected for the bulk $ZrB_2$, while the toughness at room temperature was 4.7 MPa $m^{1/2}$. The composite shows signs of plasticity at 2000 °C, where it was noted that when using the loading rate of 0.5 mm/min, the bars would not crack, yet the crack formation was noted. With an increase in the loading rate to 2.5 mm/min, the multiboride showed the very high strength of 391±14 MPa and fractured in an elastic manner. This level of strength is usually observed for the bulk zirconium diboride at room temperature. Thus, there is a distinctive positive effect of the solid-solution and composite architecture on the mechanical performance of the $ZrB_2$-based multiboride ceramic.



**Acknowledgements**

D.D. was supported by the World Premier International Research Center Initiative (WPI), MEXT, Japan. The authors deeply appreciate the urgent access to the high-temperature strength machine from Dr. Toshiyuki Nishimura (NIMS).

**References**

[1] Samsonov GV, Serebryakova TI, Neronov VA. Borides. Moscow: Atomizdat; 1975. [in Russian].

[2] Fahrenholtz WG, Hilmas GE, Talmy IG, Zaykoski JA. Refractory diborides of zirconium and hafnium. J Am Ceram Soc. 2007;90[5]:1347–1364. https://doi.org/10.1111/j.1551-2916.2007.01583.x.

[3] Brochu M, Gauntt BD, Boyer L, Loehman RE. Pressureless reactive sintering of ZrB2 ceramic. J Eur Ceram Soc. 2009;29[8]:1493–1499. https://doi.org/10.1016/j.jeurceramsoc.2008.08.032.

[4] Neuman EW, Hilmas GE, Fahrenholtz WG. Strength of zirconium diboride to 2300°C. J Am Ceram Soc. 2013;96[1]:47–50. https://doi.org/10.1111/jace.12114.

[5] Kalish D, Clougherty EV, Kreder K. Strength, fracture mode, and thermal stress resistance of HfB2 and ZrB2. J Am Ceram Soc. 1969;52[1]:30–36. https://doi.org/10.1111/j.1151-2916.1969.tb12655.x.

[6] Demirskyi D, Solodkyi I, Nishimura T, Vasylkiv O. Fracture and property relationships in the double diboride ceramic composites by spark plasma sintering of TiB2 and NbB2 J Am Ceram Soc. 2019;102[7]:4259–4271. https://doi.org/10.1111/jace.16276.

[7] Demirskyi D, Vasylkiv O. Flexural strength behavior of a ZrB2–TaB2 composite consolidated by non-reactive spark plasma sintering at 2300°C. Int J Refract Met H. 2017;66:31–35. https://doi.org/10.1016/j.ijrmhm.2017.02.003.

[8] Mroz C. Processing TiZrC and TiZrB2. Am Ceram Soc Bull. 1994;73[4]:78–81.

[9] Liu J-X, Shen X-Q, Wu Y, Li F, Liang Y, Zhang G-J, Mechanical properties of hot-pressed high-entropy diboride-based ceramics. J Adv Ceram. 2020;9:503–510. https://doi.org/10.1007/s40145-020-0383-8.

[10] Demirskyi D, Suzuki TS, Yoshimi K, Vasylkiv O. Synthesis of medium-entropy (Zr1/3Hf1/3Ta1/3)B2 using the spark plasma consolidation of diboride powders. J Ceram Soc Jpn. 2020;128[11]:977–980. https://doi.org/10.2109/jcersj2.20151.

[11] Kiessling R. The Borides of Tantalum. Acta Chem Scand. 1949;3:603–615. https://doi.org/10.3891/acta.chem.scand.03-0603.

[12] Okada S, Lundström T. Growth Conditions of Ta3B4 Single Crystals Prepared by the Aluminium-Flux Method. Bull Chem Soc Jpn. 1992;65[2]:421–423. https://doi.org/10.1246/bcsj.65.421.

[13] Okada S, Kudou K, Higashi I, Lundström T. Single crystals of TaB, Ta5B6, Ta3B4 and TAB2, as obtained from high-temperature metal solutions, and their properties. J Cryst Growth 1993;128[1-4]:1120–1124. https://doi.org/10.1016/S0022-0248(07)80109-6.

[14] Portnoi KI, Romashov VM, Salibekov SE. Constitution diagram of the system tantalum-boron. Powder Metall Met Ceram. 1971;10:925–927. https://doi.org/10.1007/BF00794010.

[15] Li J, Fan C. Novel metastable compounds in the Zr–B system: an ab initio evolutionary study. Phys Chem Chem Phys. 2015;17:1080–1088. https://doi.org/10.1039/C4CP04185B.

[16] Xie C, Zhang Q, Zakaryan HA, Wan H, Liu N, Akvashnin AG, Oganov AR. Stable and hard hafnium borides: A first-principles study. J Appl Phys. 2019;125:205109. https://doi.org/10.1063/1.5092370.

[17] Miao N, Sa B, Zhou J, Sun Z. Theoretical investigation on the transition-metal borides with Ta3B4-type structure: A class of hard and refractory materials. Comput Mater Sci. 2011;50[4]:1559–1566. https://doi.org/10.1016/j.commatsci.2010.12.015.

[18] Yao T, Wang Y, Li Hu, Lian J, Zhang J, Gou H. A universal trend of structural, mechanical and electronic properties in transition metal (M = V, Nb, and Ta) borides: First-principle calculations. Comput Mater Sci. 2012;65:302–308. https://doi.org/10.1016/j.commatsci.2012.07.021.

[19] Lu C, Gong W, Li Q, Chen C. Elucidating Stress–Strain Relations of ZrB12 from First-Principles Studies. J Phys Cgem Lett. 2020;11[21]:9165–9170. https://doi.org/10.1021/acs.jpclett.0c02656

[20] Zhang Z, Tehrani AM, Oliynyk AO, Day B, Brgoch J. Finding the Next Superhard Material through Ensemble Learning. Adv Mater. 2021;33[5]:2005112. https://doi.org/10.1002/adma.202005112.

[21] Demirskyi D, Sakka Y. High-temperature reaction consolidation of TaC-TiB2 ceramic composites by spark-plasma sintering. J Eur Ceram Soc. 2015;35[1]:405–410. https://doi.org/10.1016/j.jeurceramsoc.2014.08.007.

[22] Solodkyi I, Demirskyi D, Sakka Y, Vasylkiv O. Synthesis of multi-layered star-shaped B6O particles using the seed-mediated growth method. J Am Ceram Soc. 2015;98[12]:3635–3638. https://doi.org/10.1111/jace.13928.

[23] Demirskyi D, Vasylkiv O. Consolidation and grain growth of tantalum diboride during spark plasma sintering. Ceram Int. 2016;42[14]:16396–16400. https://doi.org/10.1016/j.ceramint.2016.07.059.

[24] Doebelin N, Kleeberg R. Profex: a graphical user interface for the Rietveld refinement program BGMN. J Appl Cryst. 2015;48:1573–1580. https://doi.org/10.1107/S1600576715014685.

[25] Newbury DE, Ritchie NWM. Performing elemental microanalysis with high accuracy and high precision by scanning electron microscopy/silicon drift detector energy-dispersive X-ray spectrometry (SEM/SDD-EDS). J Mater Sci. 2015;50:493–518. https://doi.org/10.1007/s10853-014-8685-2.

[26] Demirskyi D, Vasylkiv O. Analysis of the high-temperature flexural strength behavior of B4C–TaB2 eutectic composites produced by in situ spark plasma sintering. Mater Sci Eng A 2017;697:71–78. https://doi.org/10.1016/j.msea.2017.04.093.

[27] Demirskyi D, Vaslykiv O. Spark plasma sintering and high-temperature strength of B6O–TaB2 ceramics. J Eur Ceram Soc. 2017;37[8]:3009–3014. https://doi.org/10.1016/j.jeurceramsoc.2017.02.052.

[28] Lawn BR, Fuller ER. Equilibrium penny-like cracks in indentation fracture. J Mater Sci. 1975;10:2016–2024. https://doi.org/10.1007/BF00557479.

[29] Leone FC, Johnson NL. Statistics and Experimental Design In Engineering and the Physical Sciences. Vol 2. N.Y.: John Wiley and Sons; 1964.

[30] Andrievski RA, Spivak II. Strength of Refractory Compounds. Chelyabinsk: Metallurgiya; 1989. (in Russian).

[31] Hunter B, Yu X-X, De Leon N, et al. Investigations into the slip behavior of zirconium diboride. J Mater Res. 2016;31[18]:2749–2756. https://doi.org/10.1557/jmr.2016.201.

[32] Paul B, Okamoto NL, Kusakari M, Chen Z, Kishida K, Inui H, Otani S. Plastic deformation of single crystals of CrB2, TiB2 and ZrB2 with the hexagonal AlB2 structure. Acta Mater. 2021;221:116857. https://doi.org/10.1016/j.actamat.2021.116857.

[33] Zhang X, Hilmas GE, Fahrenholtz WG. Synthesis, densification, and mechanical properties of TaB2. Mater Lett. 2008;22[27]:4251–4353. https://doi.org/10.1016/j.matlet.2008.06.052.

[34] Demirskyi D, Badica P, Kuncser A, Vasylkiv O. Fracture peculiarities and high-temperature strength of bulk polycrystalline boron. Materialia 2022;21:101346. https://doi.org/10.1016/j.mtla.2022.101346.

[35] Wu W-W, Sakka Y, Suzuki TS, Zhang G-J. Microstructure and Anisotropic Properties of Textured ZrB2 and ZrB2–MoSi2 Ceramics Prepared by Strong Magnetic Field Alignment. Int J Appl Ceram Technol. 2014;11[2]:218–227. https://doi.org/10.1111/Ijac.12061.

[36] Lee DW, Haggerty JS. Plasticity and Creep in Single Crystals of Zirconium Carbide. J Am Ceram Soc. 1969;52[12]:641–647. https://doi.org/10.1111/j.1151-2916.1969.tb16067.x.

[37] Kelly A, Rowcliffe DJ. Slip in Titanium Carbide. Phys Stat Sol. 1966;14[1]:K29–K33. https://doi.org/10.1002/pssb.19660140132.

[38] Shaskol'skaya MP. Crystal chemistry. Moskva: Visshaya Shkola; 1984. [in Russian].

[39] Cahn RW. Plastic deformation of alpha-uranium; twinning and slip. Acta Metall. 1953;1[1]:49–52. https://doi.org/10.1016/0001-6160(53)90009-1.

[40] Cahn RW. Twinning and slip in α-uranium. Acta Cryst. 1951;4:440. https://doi.org/10.1107/S0365110X51001483.

[41] Yoo MH. Slip modes of alpha uranium. J Nucl Mater. 1968;26[3]:307–318. https://doi.org/10.1016/0022-3115(68)90104-9.

[42] Daniel JS, Lesage B, Lacombe P. Acta Metall. 1971;19[2]:163–173. https://doi.org/10.1016/0001-6160(71)90128-3.

[43] Zdaniewski WA. Solid Solubility Effect on Properties of Titanium Diboride. J Am Ceram Soc. 1987;70[11]:793–797. https://doi.org/10.1111/j.1151-2916.1987.tb05630.x.

[44] Glaser FW. Contribution to the Meta I-Carbon-Boron Systems. JOM 1952;4:391–396. https://doi.org/10.1007/BF03397703.

[45] Rudy E, Benesovsky F. Untersuchungen in den Systemen: Hafnium—Bor—Stickstof und Zirkonium—Bor—Stickstoff. Monatsh Chem. 1961;92:415–441. https://doi.org/10.1007/BF01153900

[46] Nowotny H, Rudy E, Benesovsky F. Untersuchungen in den Systemen: Zirkonium-Bor-Kohlenstoff und Zirkonium-Bor-Stickstoff. Monatsh Chem. 1960;91:963–974. https://doi.org/10.1007/BF00929564.

[47] Ding H-J, Wang X-G, Xia J-F, Bao W-C, Zhang G-J, Zhang C, Jiang D-Y. Effect of solid solution and boron vacancy on the microstructural evolution and high temperature strength of W-doped ZrB2 ceramics. J Alloy Compd. 2020;827:154293. https://doi.org/10.1016/j.jallcom.2020.154293.

[48] Andrievskii RA, Lanin AG, Rymashevskii GA. The Strength of Refractory Compounds. Moscow:Metallurgiya;1974. [in Russian].

[49] Brewer L, Haraldsen H. The Thermodynamic Stability of Refractory Borides. J Electrochem Soc. 1955;102[7]:399–407. https://doi.org/10.1149/1.2430108.

[50] Demirskyi D, Solodkyi I, Nishimura T, Sakka Y, Vasylkiv O. High-temperature strength and plastic deformation behavior of niobium diboride consolidated by spark plasma sintering. J Am Ceram Soc. 2017;100[11]:5295–5305. https://doi.org/10.1111/jace.15048.

[51] Wang YC, Fu ZY. Study of temperature field in spark plasma sintering. Mater Sci Eng B 2002;90[1–2]: 34–37. https://doi.org/10.1016/S0921-5107(01)00780-2.

[52] Demirskyi D, Suzuki TS, Grasso S, Vasylkiv O. Microstructure and flexural strength of hafnium diboride via flash and conventional spark plasma sintering. J Eur Ceram Soc. 2019;39[4]:898–906. https://doi.org/10.1016/j.jeurceramsoc.2018.12.012.

[53] Dzyadykevych Y, Smiyan O. Investigation of the initial stage of borating tantalum. Int J Refract Met Hard Mater. 2007;25[5–6]:361–366. https://doi.org/10.1016/j.ijrmhm.2007.01.001.

[54] Chamberlain AL, Fahrenholtz WG, Hilmas GE. Pressureless sintering of zirconium diboride. J Am Ceram Soc. 2006;89[2]:450–456. https://doi.org/10.1111/j.1551-2916.2005.00739.x.

[55] Zapata-Solvas E, Jayaseelan DD, Lin HT, Brown P, Lee WE. Mechanical properties of ZrB2- and HfB2-based ultra-high temperature ceramics fabricated by spark plasma sintering. J Eur Ceram Soc. 2013;33[7]:1373–1386. https://doi.org/10.1016/j.jeurceramsoc.2012.12.009.

[56] Sciti D, Nygren M. Spark plasma sintering of ultra refractory compounds. J Mater Sci. 2008;43:6414–6642. https://doi.org/10.1007/s10853-008-2718-7.

[57] Verma V, Cheverikin V, Cozza RC. Review: effect on physical, mechanical and wear performance of ZrB2 based composites processed with or without additives. Int J Appl Ceram Technol. 2020;17:2509–2532. https://doi.org/10.1111/ijac.13567.

[51] Ivan'ko AA. Hardness. Kiev: Naukova Dumka; 1968. [in Russian].

[59] Qin M, Yan Q, Liu Y, Luo J. A new class of high-entropy M3B4 borides. J Adv Ceram. 2021;10[1]:166–172. https://doi.org/10.1007/s40145-020-0438-x.

[60] Itoh H, Satoh Y, Kodama S, Naka S. Synthesis of Tantalum Boride Powder by Solid State Reaction and Its Sintering. J Ceram Soc Jpn. 1990;98[1135]:264–268. https://doi.org/10.2109/jcersj.98.264.

[61] Chung H-Y, Weinberger MB, Levine JB, et al. Synthesis of ultra-incompressible superhard rhenium diboride at ambient pressure. Science 2007;316[5823]:436–439. https://doi.org/10.1126/science.1139322.

[62] Neuman E, Hilmas GE, Fahrenholtz WG. Ultra-high temperature mechanical properties of a zirconium diboride–zirconium carbide ceramic. J Am Ceram Soc. 2016;99[2]:597–603. https://doi.org/10.1111/jace.13990.

[63] Baumgartner HR, Steiger RA. Sintering and properties of titanium diboride made from powder synthesized in a plasma-arc heater. J Am Ceram Soc 1984;67[3]:207–212. https://doi.org/10.1111/j.1151-2916.1984.tb19744.x.

[64] Filatov SK. High-temperature crystal chemistry. Leningrad: Nedra; 1990. [in Russian].

[65] Demirskyi D, Nishimura T, Sakka Y, Vasylkiv O. High-strength TiB2–TaC ceramic composites prepared using reactive spark plasma consolidation. Ceram Int. 2016;42[14]:1298–1306. https://doi.org/10.1016/j.ceramint.2016.07.059.

[66] D'Angio A, Zou J, Binner J, Ma H-B, Hilmas GE, Fahrenholtz WG. Mechanical properties and grain orientation evolution of zirconium diboride-zirconium carbide ceramics. J Eur Ceram Soc. 2018;38[2]:391–402. https://doi.org/10.1016/j.jeurceramsoc.2017.09.013.

[67] Mullins WW. Theory of Thermal Grooving. J Appl Phys. 1956;28[3]:333–339. https://doi.org/10.1063/1.1722742.

[68] Hayami W, Souda R, Aizawa T, Tanaka T. Structural analysis of the HfB2 (0001) surface by impact-collision ion scattering spectroscopy. Surf Sci. 1998;415[3]:433–437. https://doi.org/10.1016/S0039-6028(98)00618-9.

[69] Futamoto M, Nakazawa M, Usami K, Hosoki S, Kawabe U. Thermionic emission properties of a single- crystal LaB6 cathode. J Appl Phys. 1980;51[7]:3869–3876. https://doi.org/10.1063/1.328132.

[70] Anderson MW, Gebbie-Rayet JT, Hill AR, et al. Predicting crystal growth via a unified kinetic three-dimensional partition model. Nature 2017;544:456–459. https://doi.org/10.1038/nature21684.

[71] Kalish D, Clougherty EV. Densification Mechanisms in High-pressure Hot-Pressing of HfB2. J Am Ceram Soc. 1969;52[1]:26–30. https://doi.org/10.1111/j.1151-2916.1969.tb12654.x.

[72] Leitnaker JM, Bowman MG, Gilles PW. Thermodynamic Properties of the Tantalum and Tungsten Borides. J Electrochem Soc. 1962;109[5]:441–443. https://doi.org/10.1149/1.2425442.

[73] Haggerty JS, Lee DW. Plastic Deformation of ZrB2 Single Crystals. J Am Ceram Soc. 1971;54[11]:572–576. https://doi.org/10.1111/j.1151-2916.1971.tb12210.x.

[74] D. Ghosh, G. Subhash, G.R. Bourne, Room-temperature dislocation activity during mechanical deformation of polycrystalline ultra-high-temperature ceramics, Scr Mater. 2009;61[11]:1075–1078. https://doi.org/10.1016/j.scriptamat.2009.08.038.

[75] Neuman EW, Hilmas GE, Fahrenholtz WG. Elevated Temperature Strength Enhancement of ZrB2–30 vol% SiC Ceramics by Postsintering Thermal Annealing. J Am Ceram Soc. 2016;99[3]:962–970. https://doi.org/10.1111/jace.14029.

[76] Silvestroni L, Kleebe HJ, Fahrenholtz WG, Watts J. Super-strong materials for temperatures exceeding 2000 °C. Sci Rep 2017;7:40730. https://doi.org/10.1038/srep40730.

[77] Silvestroni L, Sciti D, Monteverde F, Stricker K, Kleebe H-J. Microstructure evolution of a W-doped ZrB2 ceramic upon high-temperature oxidation. J Am Ceram Soc. 2017;100[4]:1760–1772. https://doi.org/10.1111/jace.14738.

[78] Ma H-B, Zou J, Zhu J-T, Liu L-F, Zhang G-J. Segregation of tungsten atoms at ZrB2 grain boundaries in strong ZrB2-SiC-WC ceramics. Scr Mater. 2018;157:76–80. https://doi.org/10.1016/j.scriptamat.2018.07.038.

[79] Dai F-Z, Wen B, Xiang H, Zhou Y. Grain boundary strengthening in ZrB2 by segregation of W: Atomistic simulations with deep learning potential. J Eur Ceram Soc. 2020;40[15]:5029–5036. https://doi.org/10.1016/j.jeurceramsoc.2020.06.007.

## Tables

**Table 1**. Crystallographic and mechanical details on multiboride composite constituent phases.

| Compound | Crystal structure[30] | Space group (space group number) | Young's Modulus, GPa[1] | Hardness, GPa | Main slip-system | |
|---|---|---|---|---|---|---|
| | | | | | Low-temperature | High-temperature |
| $ZrB_2$ | Hexagonal | *P6/mmm* (#191) | 440 [31] | 14.5±0.7[3][35] | {1010}<1120> {0001}<11-20>[30,31] | {1-100}<11-23>[32] |
| $TaB_2$ | Hexagonal | *P6/mmm* (#191) | 551±8 [33] | 25.5 [2][14] 25.6 [5][33] | | |
| ZrB | Cubic | *Fm-3m* (#225) | N.A. | | {100}[6][30,36,37] | {111}<1-10>[30,36,37] |
| TaB | Orthorhombic | *Cmcm* (#63) | N.A. | 20.0 [2][14] | {010}<100>[8] [39–42] | N.A. |
| $Ta_3B_4$ | Orthorhombic | *Immm* (#71) | N.A. | 24.0 [2][14] | NA[7][38] | N.A. |
| β-Boron | Trigonal | R-3m (#166) | 442±18 [28] | 32.3 [2][14] 32.1±0.6 [4][34] | Basal slip {0001}<11-20>[34] | Prismatic slip {1-210}<10-10>[34] |

Notes:
N.A. – not available (not reported at the time of submission of the manuscript)
1 at room-temperature
2 using 0.49 N load
3 using 49 N load
4 using 9.8 N load
5 using 4.9 N load
6 based on the ZrC with *Fm-3m* structure
7 most likely {100} at room-temperature according to ref. [38]
8 [39]–[42] based on the low-temperature brittle fracture of α-U with *Cmcm* structure

**Table 2**. Elevated temperature mechanical properties of Zr–Ta multiboride, and $ZrB_2$ [4] and $ZrB_2$–$TaB_2$ composite [7].

| Temperature, °C | Flexural strength, MPa (crosshead rate, mm/min) | | |
|---|---|---|---|
| | $ZrB_2$-C [4] | $ZrB_2$–$TaB_2$ [7] | Multiboride [this study] |
| 25 | 381±41 (0.5) | 393±29 (0.5) | 493±19 (0.5) |
| 1000 | 399±37 (0.5) | 401±27 (0.5) | 625±26 (0.5) |
| 1600 | 212±26 (2.0) | 336±23 (0.5) | 457±23 (0.5) |
| 1800 | 220±18 (2.5) | 256±13 (0.5) | 354±30 (0.5) |
| 2000 | 223±18 (2.5) | | 240±20 (0.5)* |
| 2000 | | | 391±14 (2.5) |

* the value is for yield stress (see **Fig. 8**).

**Figure captions**

**Figure 1**. Response surface representation of the (a) room temperature flexural strength and (b) hardness using the two-step SPS processing. The x-axis is the dwell being used for consolidation, while the y-axis is the dwell at 1400°C that is being used at the cooling stage in order to control strain induced by the difference in the coefficient of the thermal expansion of boride phases. Dotted lines show the 20/5 configuration used for the preparation of the multiboride ceramic composite used for the high-temperature flexural tests. Hardness was evaluated using a 196 N load. The strength was evaluated using a three-point flexural test.

**Figure 2**. Representative microstructure of the multiboride ceramic after consolidation at 1900 °C. Black areas are unreacted boron and pores. Right image shows an overlay of Ta (blue) and Zr (red) maps after the EDS.

**Figure 3**. X-ray diffraction pattern observed after the SPS consolidation. Vertical lines indicate the Bragg position for the boride phases. Red solid line shows the refinement performed using the Rietveld method. ($\chi^2$ – 2.06, GoF – 1.44). Initial structures used during the refinement process can be obtained using the Crystallography Open Database (COD) number.

**Figure 4**. Schematic formation of the phases during the reaction and cooling stages of the consolidation process. Note that the Ta-B mixture was prepared, then the $ZrB_2$ was added the mixture. The inset shows the area where the TaZrB phase is being formed, while the main phase is the diboride solid-solution. Such a scenario is only possible in the ideal mixing case.

**Figure 5**. The hardness of multiboride and $ZrB_2$ [35,54–56] as a function of load*. Insets illustrate the multiboride samples indented with loads of 98 N and 196 N.

*PS – pressureless sintering; HP – hot pressing; SPS – spark plasma sintering.

**Figure 6**. Macroscopic fracture details on the flexure of the multiboride ceramic composite at 2000 °C using a 0.5 mm/min loading rate. Representative fracture at 2000 °C using a 2.5 mm/min loading rate using SE and BSE images. Inset shows the loading procedure during the three-point flexural strength test.

**Figure 7**. Representative fracture of the multiboride ceramics during the flexure at 1800 °C.

**Figure 8**. Effect of temperature of the flexural test on the fracture behavior of the multiboride ceramic using a loading rate of 0.5 mm/min. The right-bottom image shows the typical shape of the strain-stress curves using loading rate of 0.5 mm/min and 2.5 mm/min at 2000 °C (solid red line).

**Figure 9.** Fracture of the multiboride ceramic composite at 2000 °C when a $ZrB_2$ grain has a shape typical of the {0001} plane. Right images and the inset for $ZrB_2$ show formation of the step-like or terrace structure during the surface grooving process for borides at 2000 °C. These images illustrate the formation of the grooving steps (growth steps) during the exposure of the various borides to temperature of 2000 °C. See *Suppl. S5* and *video files* for details.

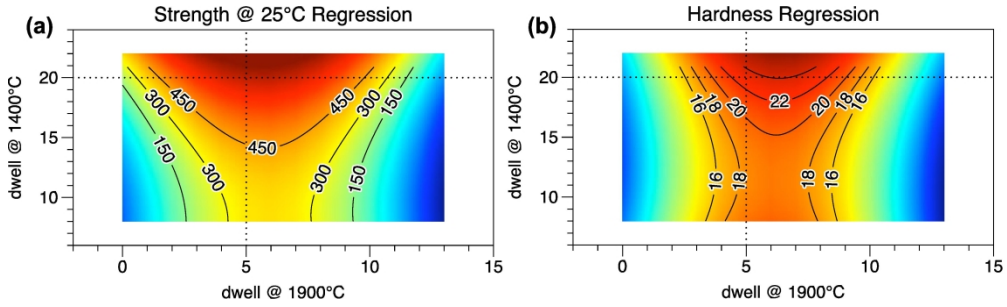


Figure 1. Response surface representation of the (a) room temperature flexural strength and (b) hardness using the two-step SPS processing. The x-axis is the dwell being used for consolidation, while the y-axis is the dwell at 1400°C that is being used at the cooling stage in order to control strain induced by the difference in the coefficient of the thermal expansion of boride phases. Dotted lines show the 20/5 configuration used for the preparation of the multiboride ceramic composite used for the high-temperature flexural tests. Hardness was evaluated using a 196 N load. The strength was evaluated using a three-point flexural test.

185x54mm (600 x 600 DPI)

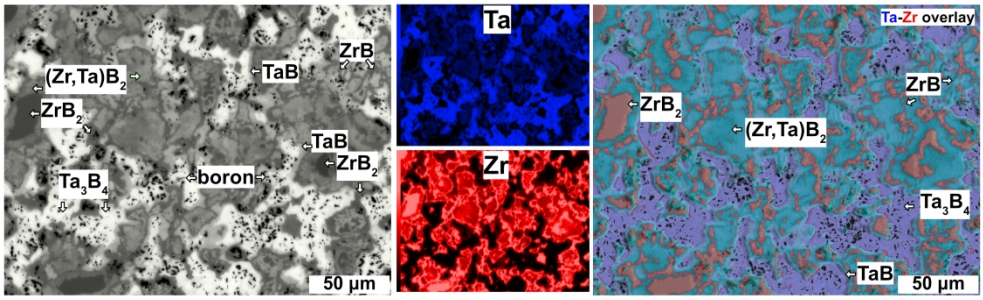


Figure 2. Representative microstructure of the multiboride ceramic after consolidation at 1900 °C. Black areas are unreacted boron and pores. Right image shows an overlay of Ta (blue) and Zr (red) maps after the EDS.

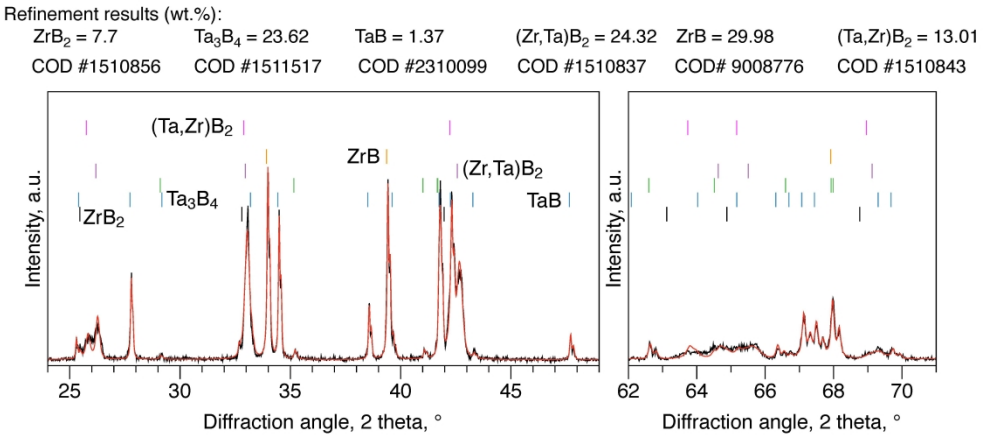


Figure 3. X-ray diffraction pattern observed after the SPS consolidation. Vertical lines indicate the Bragg position for the boride phases. Red solid line shows the refinement performed using the Rietveld method. (χ2 – 2.06, GoF – 1.44). Initial structures used during the refinement process can be obtained using the Crystallography Open Database (COD) number.

208x101mm (600 x 600 DPI)

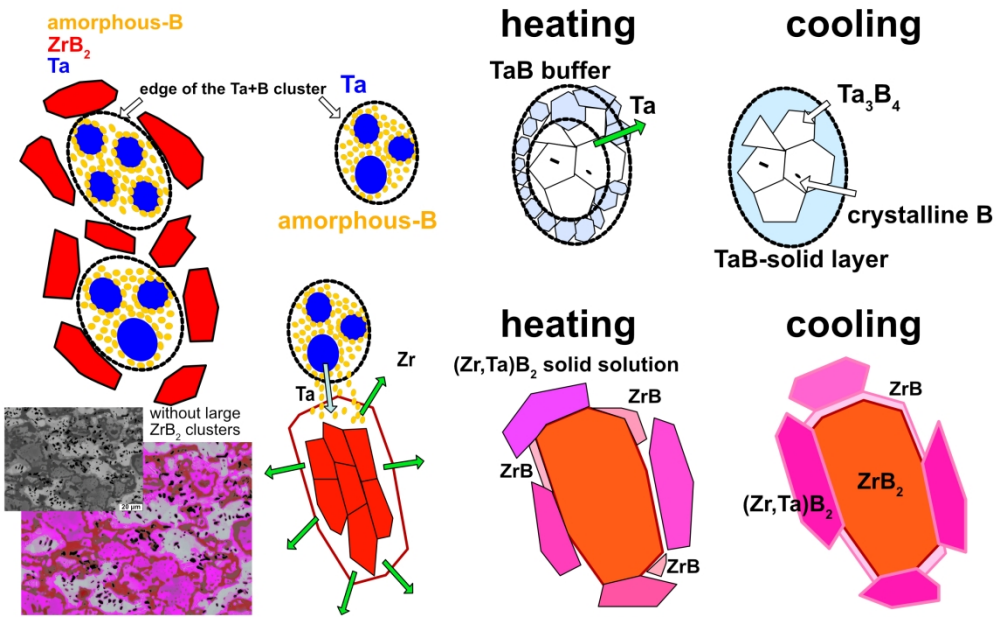


Figure 4. Schematic formation of the phases during the reaction and cooling stages of the consolidation process. Note that the Ta-B mixture was prepared, then the ZrB2 was added the mixture. The inset shows the area where the TaZrB phase is being formed, while the main phase is the diboride solid-solution. Such a scenario is only possible in the ideal mixing case.

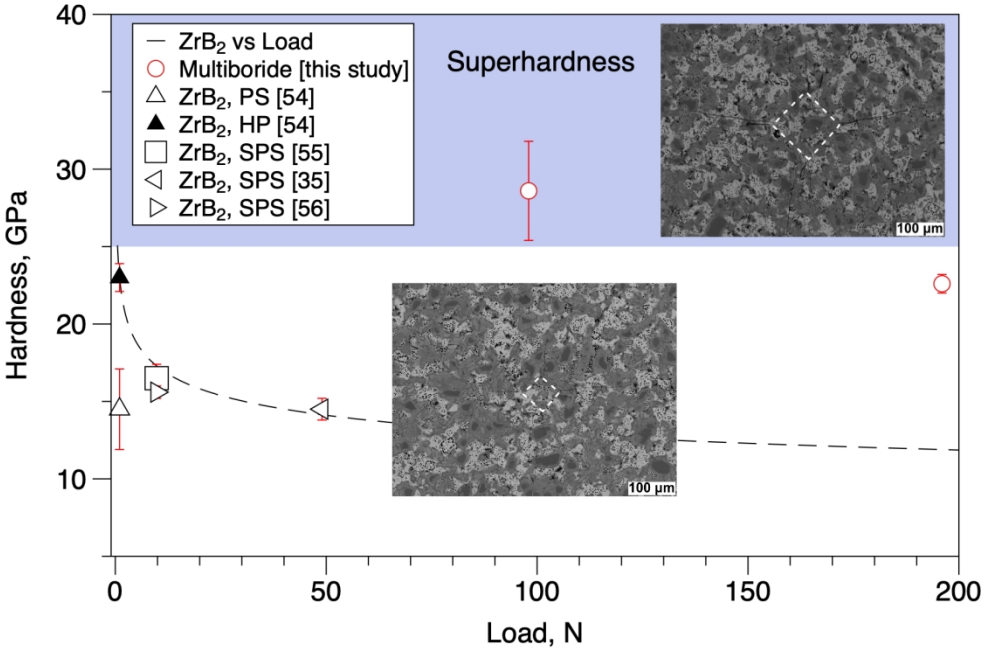


Figure 5. The hardness of multiboride and ZrB2 [35,54–56] as a function of load*. Insets illustrate the multiboride samples indented with loads of 98 N and 196 N.

152x101mm (300 x 300 DPI)

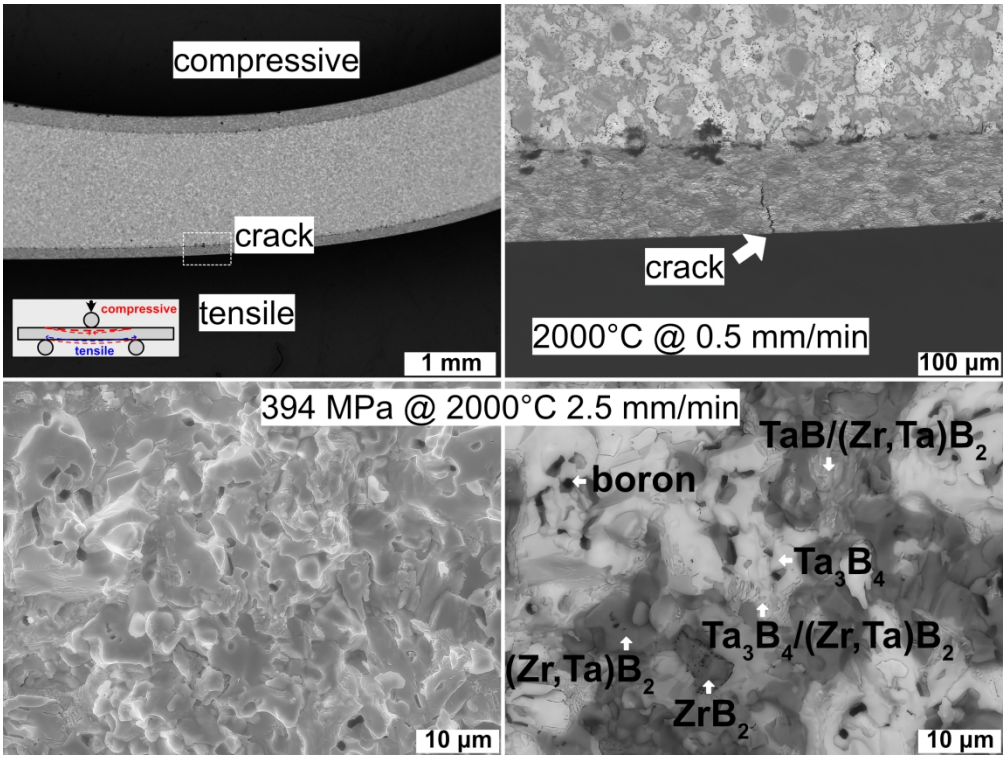


Figure 6. Macroscopic fracture details on the flexure of the multiboride ceramic composite at 2000 °C using a 0.5 mm/min loading rate. Representative fracture at 2000 °C using a 2.5 mm/min loading rate using SE and BSE images. Inset shows the loading procedure during the three-point flexural strength test.

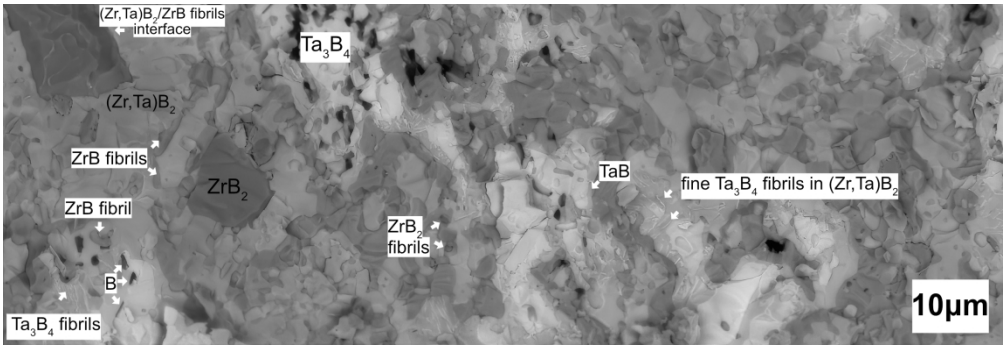


Figure 7. Representative fracture of the multiboride ceramics during the flexure at 1800 °C.

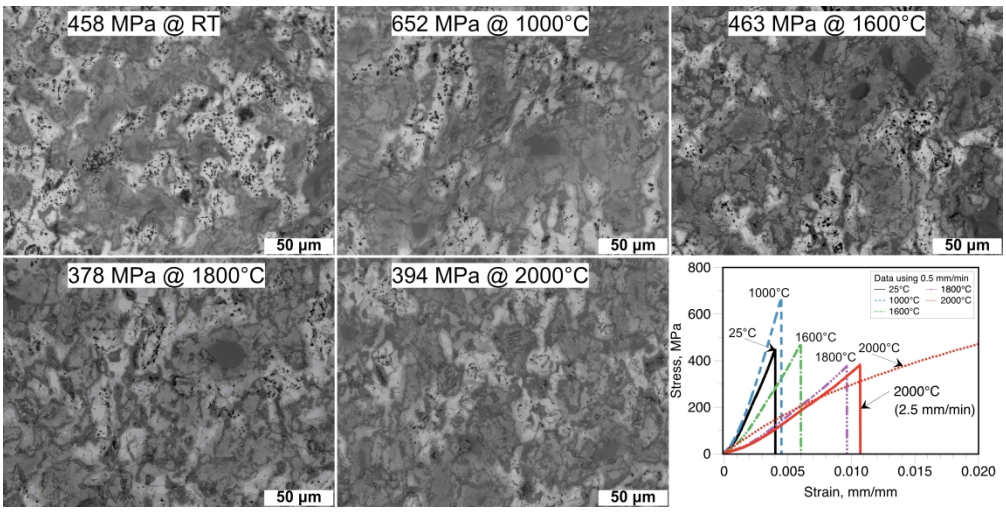


Figure 8. Effect of temperature of the flexural test on the fracture behavior of the multiboride ceramic using a loading rate of 0.5 mm/min. The right-bottom image shows the typical shape of the strain-stress curves using loading rate of 0.5 mm/min and 2.5 mm/min at 2000 °C (solid red line).

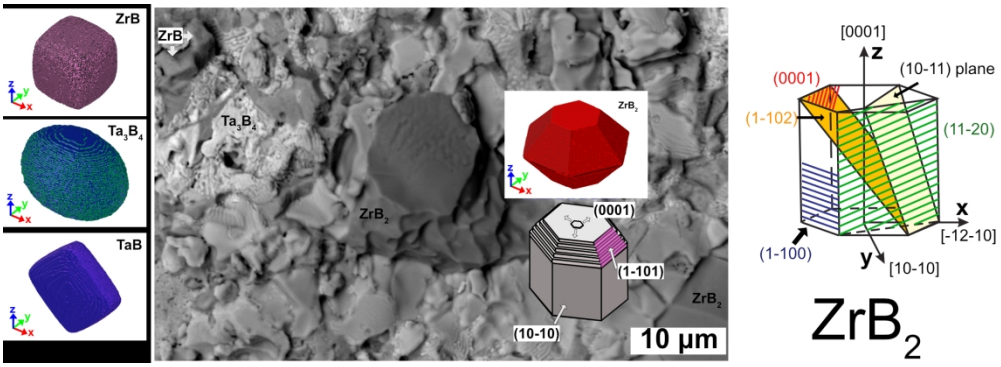


Figure 9. Fracture of the multiboride ceramic composite at 2000 °C when a ZrB2 grain has a shape typical of the {0001} plane. Right images and the inset for ZrB2 show formation of the step-like or terrace structure during the surface grooving process for borides at 2000 °C. These images illustrate the formation of the grooving steps (growth steps) during the exposure of the various borides to temperature of 2000 °C. See Suppl. S5 and video files for details.

# Supporting Information

## High-temperature reactive synthesis of the Zr-Ta multiboride with a supercomposite structure

D. Demirskyi (a,b,c)†, T.S. Suzuki(b), K. Yoshimi (c), O. Vasylkiv (b)†.

(a) WPI-Advanced Institute for Materials Research (WPI-AIMR), Tohoku University, 2-1-1 Katahira, Aoba-ku, Sendai, 980-8577 Japan

(b) National Institute for Materials Science, 1-2-1 Sengen, Tsukuba, Ibaraki 305-0047, Japan

(c) Department of Materials Science and Engineering, Tohoku University, 6-6-02 Aramaki Aza Aoba, Sendai, 980-8579, Japan

E-mail: demirskyi.dmytro.e2@tohoku.ac.jp, oleg.vasylkiv@nims.go.jp.

**Appendix**

**Supporting information, S1.** ***Design of the SPS experiments***

In order to find an optimal strength at room temperature, a number of the SPS runs were performed. In order to determine the nature of the surface response using few experiments as possible, a factorial design with additional center point was used [R1].

**Tables T1** and **T2** reveal the coding and the experimental parameters used within this study. Initial parameters *x1* and *x2* were based on the 10-mm diameter runs using a similar strategy. Using the 10/5 configuration for the 10-mm specimens resulted in the structure where the majority of the $ZrB_2$ had a shape of the quasi-continuous fiber.

After completing 15 SPS runs specimens were checked for three criteria: (1) presence of cracks; (2) hardness of the composite and (3) flexural strength at room temperature. For the two latter parameters we evaluated a response surface based on the initial data [R1]. **Figure F1** shows the contours for the linear regression performed using strength data. These were performed by a single test per specimen. To simplify the hardness evaluation procedure, only load of a 196 N was used, and these indents were easily observed and measured by the optical microscopy. Thus, the **Figure F2** illustrates the response surface representation of the Vickers hardness (196 N load), while the specimens used for the high-temperature properties specimen showed Vickers hardness of 22.6±0.6 GPa (196 N load). Note, that the average value

of the strength for a selected '20/5' specimen used for the high-temperature strength was 499±28 MPa at room temperature (based on the seven tests).

The response surfaces presented in **Figs. F1,F2** can be analyzed as follows: a dwell at 1400 °C is responsible for equilibration of the thermal stresses caused by the cooling from the 1900 °C. The latter temperature was found to satisfy the minor growth of the phases while producing almost pore-free specimen. The response surface presented in **Figs. F1,F2** suggests that (i) a lengthy dwell is required at 1400 °C and (ii) a maximum in the hardness or strength may lie outside of the experimental design used in **Table T2**. Some specimens with *x2* higher than 6 min had macroscopic cracks and could not be considered for the high-temperature tests. Because the microstructure or XRD showed no reasonable difference between these runs and with lower with *x2* being than 6 min one can expect that only in-depth analysis will allow one to explain the macro-cracking. Note, that similar to the ceramic prepared using 20/5 composition the $ZrB_2$ remained highly strained in all specimens.



**Table T1**. Parameters used in the design of the experiment*

| Parameter (code) | Dwell at 1400°C (x1) | Dwell at 1900°C (x2) |
|---|---|---|
| Zero value, min | 10 | 6 |
| Step, min | 10 | 4 |

* Initial values for the optimum processing parameters based on the 10-mm runs

**Table T2.** The design of the experiment for the consolidation of the multiboride ceramic composites

| SPS run ID | Dwell at 1400°C | Dwell at 1900°C | x1 | x2 |
|---|---|---|---|---|
| 1 | 0 | 2 | -1 | -1 |
| 2 | 0 | 10 | -1 | 1 |
| 3 | 20 | 2 | 1 | -1 |
| 4 | 20 | 10 | 1 | 1 |
| 5 | 0 | 2 | -1 | -1 |
| 6 | 0 | 10 | -1 | 1 |
| 7 | 20 | 2 | 1 | -1 |
| 8 | 20 | 10 | 1 | 1 |
| 9 | 10 | 6 | 0 | 0 |
| 10 | 10 | 6 | 0 | 0 |
| 11 | 18 | 4 | 0.8 | -0.5 |
| 12 | 18 | 8 | 0.8 | 0.5 |
| 13 | 13 | 4 | 0.3 | -0.5 |
| 14 | 13 | 8 | 0.3 | 0.5 |
| 15 | 10 | 6 | 0 | 0 |

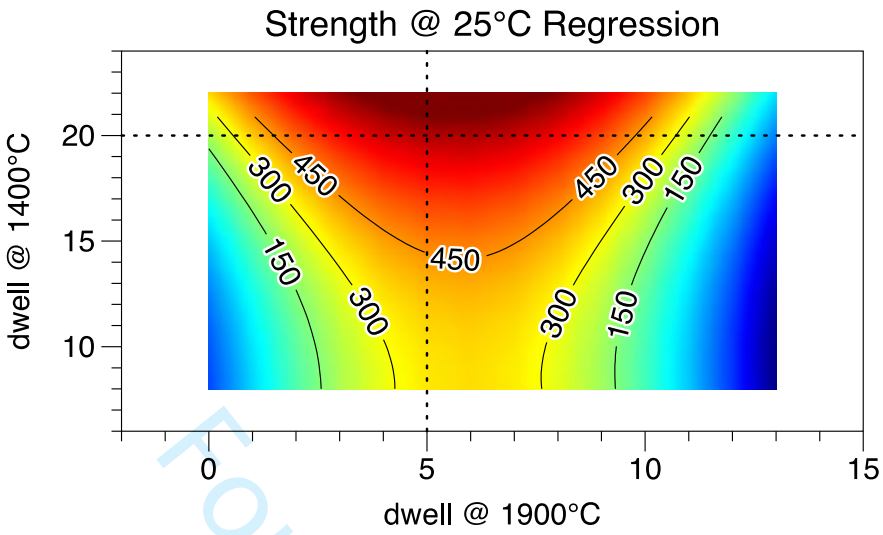


**Figure F1**. Response surface representation of the room temperature flexural strength using the two-step SPS processing. Dotted lines show the 20/5 configuration. The strength was evaluated using a three-point flexural test.

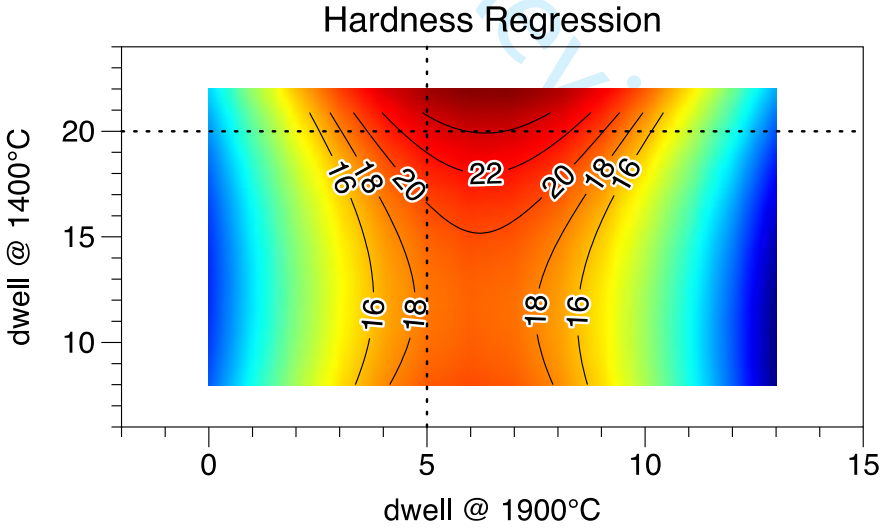


**Figure F2**. Response surface representation of the Vickers hardness using the two-step SPS processing. Dotted lines show the 20/5 configuration. Hardness was evaluated using a 196 N load.

## Supporting information, S2. *Anisotropy in Young's moduli*

The elastic moduli for borides in Zr-Ta multiboride can be calculated and visualized using ELATE or AnisoVis [R2]. Elastic tensor matrices for $ZrB_2$, ZrB, TaB and $Ta_3B_4$ were obtained through Materials Project [R3]. These matrices were calculated using density functional theory methods and have not been confirmed experimentally. **Table T3** contains information on anisotropy, minimum and maximum Young's moduli. **Figures F3** and **F4** present three-dimensional and planar projections of the Young's moduli for these borides. It is important to emphasize that for an ideal isotropic crystal the three-dimensional projection of the Young modulus is a sphere (in 2D it is a circle).

**Table T3**. Variations of the elastic moduli for selected borides

| Compound | Young's modulus, GPa | | Anisotropy |
|---|---|---|---|
| | $E_{min}$ | $E_{max}$ | |
| $ZrB_2$ | 378 | 550 | 1.45 |
| ZrB | 138 | 338 | 2.45 |
| TaB | 415 | 570 | 1.37 |
| $Ta_3B_4$ | 394 | 555 | 1.40 |

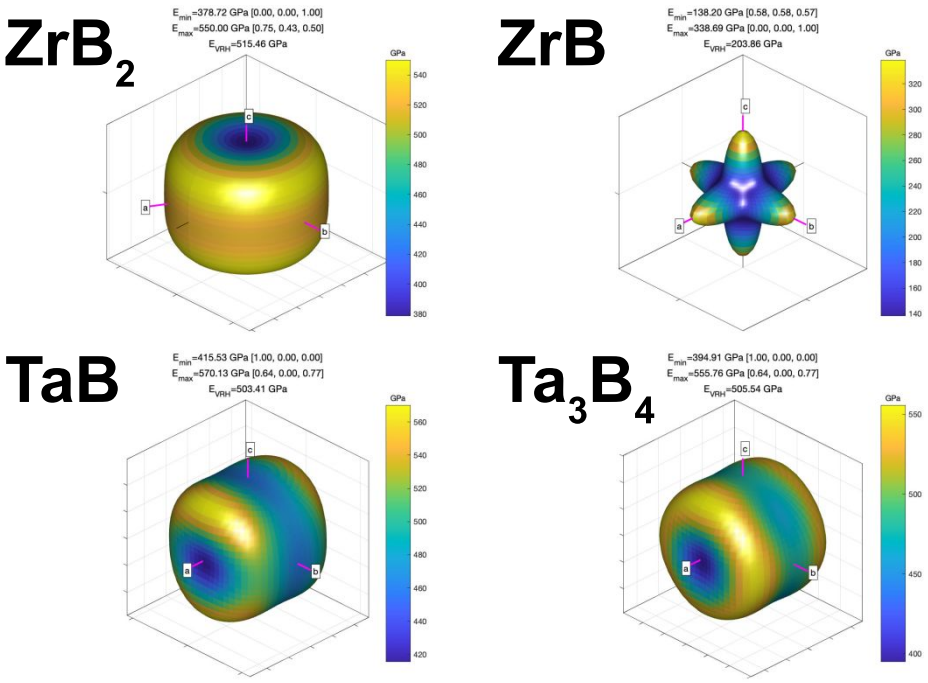


**Figure F3**. 3D visualization the Young's modulus for selected borides. The scale bar is not normalized, and the minimum/maximum level is calculated individually for each boride.

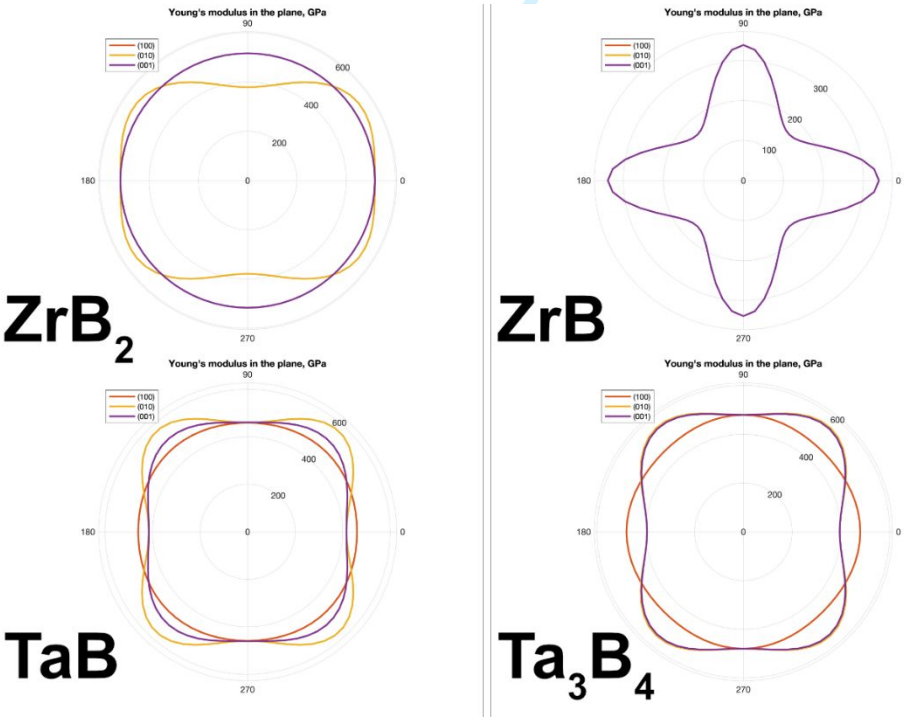


**Figure F4**. Spatial dependence of Young's modulus for selected borides.

**Supporting information, S3.** ***Interpretation of the composite macrostructure***

After examination of the polished surface using the optical microscopy, we found that there was a regular cell-chain structure (**Figure F5**) with a solid-solution phase entrapped with a quasi-continuous chain-like layer of the $Ta_3B_4$/TaB. SEM observation using similar magnification (×50), confirmed these observations (**Figure F6**)[R4]. Overall, the solid-solutions between zirconium and tantalum dibordies and $Ta_3B_4$/TaB clusters form a structure where these phases are evenly distributed. Hence, we consider that the multiboride composite has a hierarchical superstructure.

Mechanical properties should *de facto* benefit from formation of the superstructure as formation of a regular composite structure allows increase in the strength or toughness from an interaction of the crack-tip with a composite. Typical mechanisms that are anticipated to contribute to the improvement of the mechanical properties are illustrated in **Figure F7**. We should underline that this is a schematic diagram, and thus is an oversimplification of the real composite structure and we expect that the microcrack tip-shielding should lead to increase in the strength/toughness at the elevated temperatures. As one can see in **Figure F8** the localized microstructure after flexural strength may include fiber-like ZrB/$ZrB_2$ grains. Furthermore, the solid-solution and $Ta_3B_4$ phases interpenetrate each other creating an additional barrier for the crack propagation.


**Figure F5**. Structure of the multiboride ceramic composite after spark plasma sintering at 1900 °C by an optical microscope. Chain-cell structure can be observed.

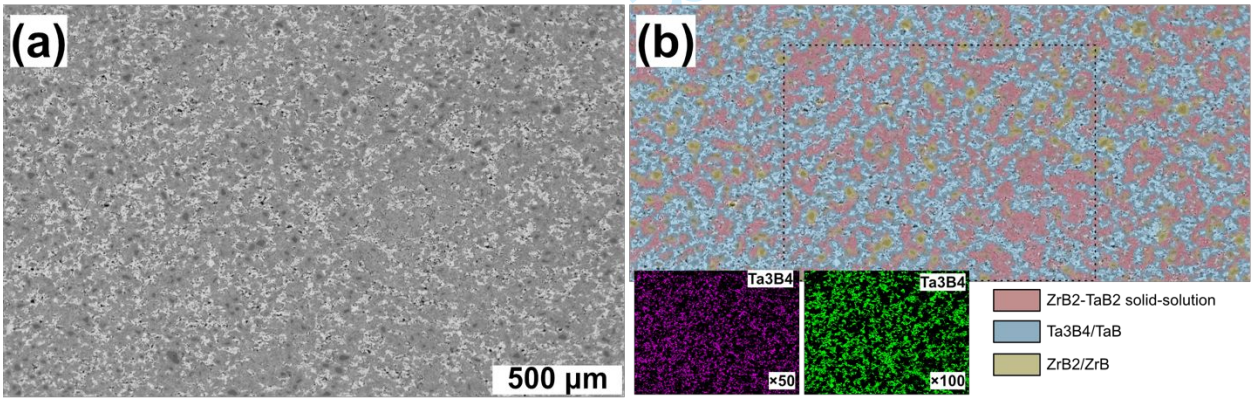


**Figure F6**. Structure of the multiboride ceramic after consolidation at 1900 °C. (b) shows automatic segmentation performed by the self-learning engine [R4]. Dotted square in (b) is for the area used for $Ta_3B_4$ map using ×100 magnification.

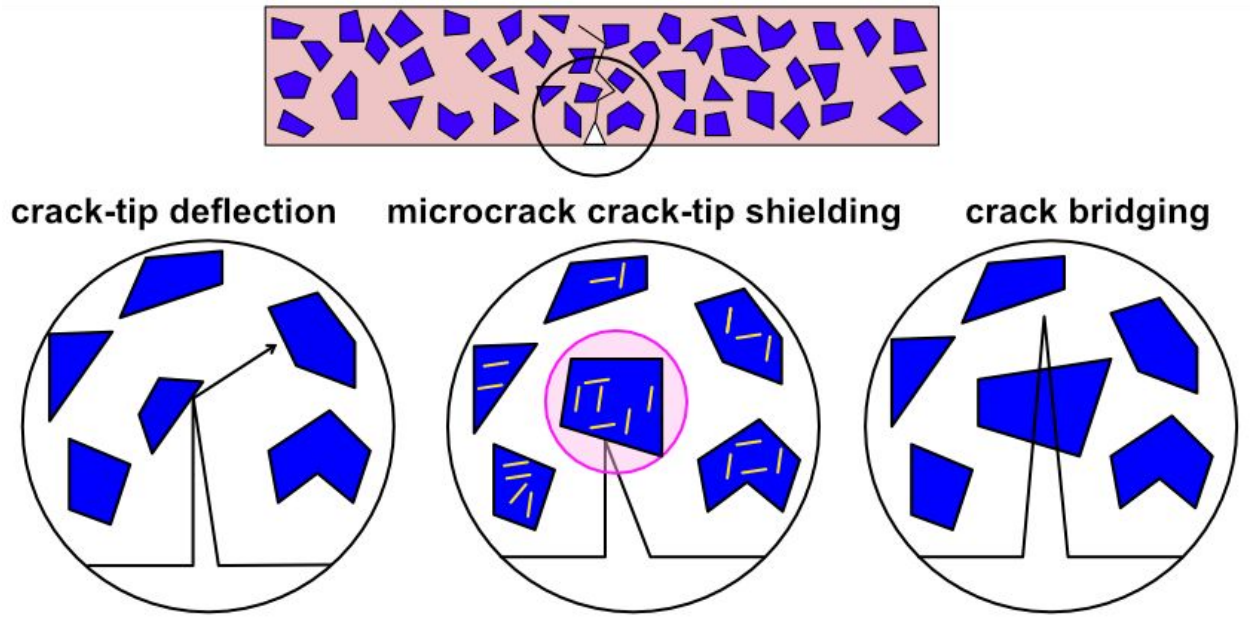


**Figure F7**. Schematic diagram illustrating the possible strengthening/toughening mechanisms in the multiboride ceramic composite.

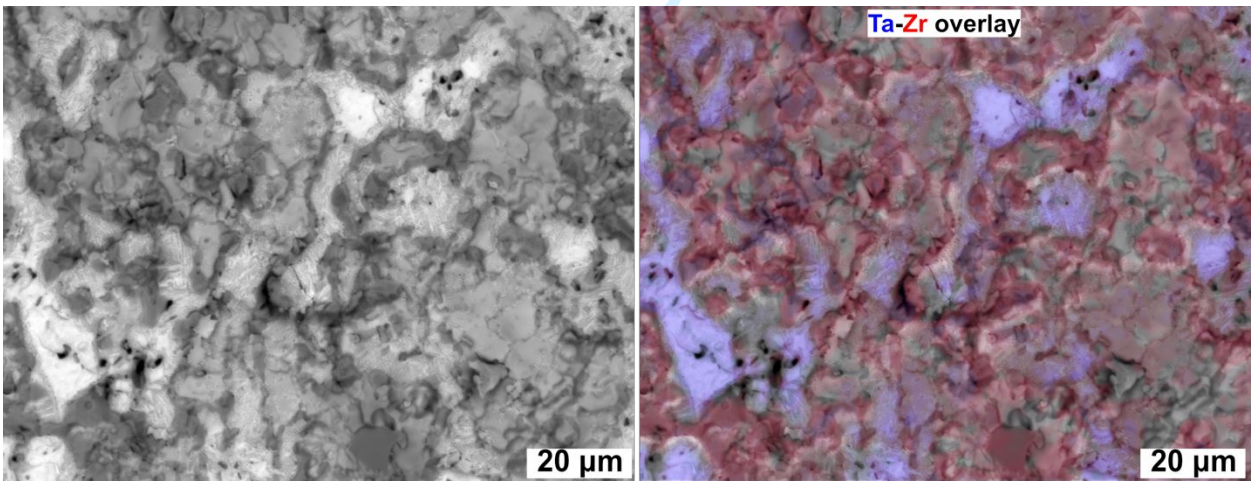


**Figure F8**. Representative fracture of the multiboride ceramic after flexural tests at 2000 °C. Black areas are boron, grain pull-outs and pores.

## Supporting information, S4. *Indentation fracture toughness*

The indentation fracture toughness ($K_{IC}$) was evaluated using three different equations (**Table T4**) [R5–R7]. Typical crack observed during the indentation tests is presented in **Figure F9**. The fracture toughness using the flexure approach showed a value of 4.7 MPa $m^{1/2}$ at room temperature. The $K_{IC}$ was best estimated by eq. 1 which yielded the toughness between 4.0 and 4.8 MPa $m^{1/2}$.

**Table T4**. Equations for calculation of the indentation fracture toughness ($K_{IC}$)

| Eq # | Equation | Ref. | Toughness, MPa $m^{1/2}$ Median /Average |
|---|---|---|---|
| 1 | $K_{IC} = 0.073\ (P/c^{3/2})$ | [R5] | 4.4; 4.6 |
| 2 | $K_{IC} = 0.016(E/HV)^{1/2}\ (P/c^{3/2})$ | [R6] | 4.7; 4.8 |
| 3 | $K_{IC} = 9.052\ 10^{-3}\ HV^{3/5}\ E^{2/5}\ 2a\ c^{-1/2}$ | [R7] | 6.8; 7.1 |

where *P* is the load, *HV* is the Vickers hardness, *E* is Young's modulus (480 GPa), *2a* is the diagonal of the indentation, and *c* is the crack length.

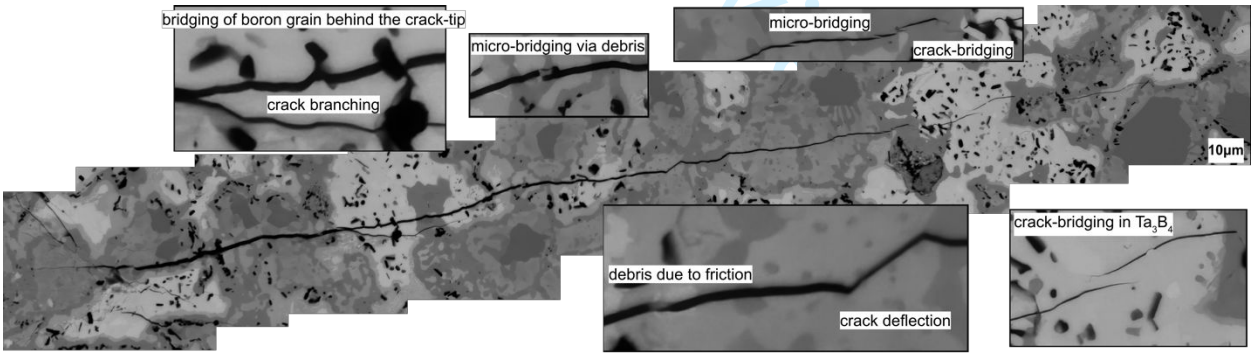


**Figure F9**. Representative crack propagation in the multiboride ceramic after the indentation test using a 196 N load.

**Supporting information, S5.** ***Evolution of the surface during the crystal growth***

Video files with titles SVideo1, SVideo2, SVideo3 and SVideo4 were prepared by Ovito [R8] using the simulation output by CrystalGrower [R9] for $Ta_3B_4$, TaB, ZrB and $ZrB_2$, respectively.

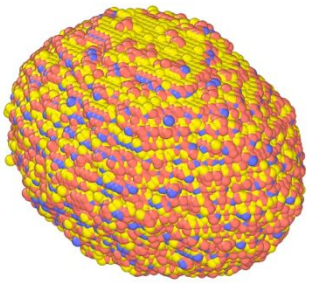


SVideo1. Surface evolution of $Ta_3B_4$ crystal during exposure to 2000 °C.

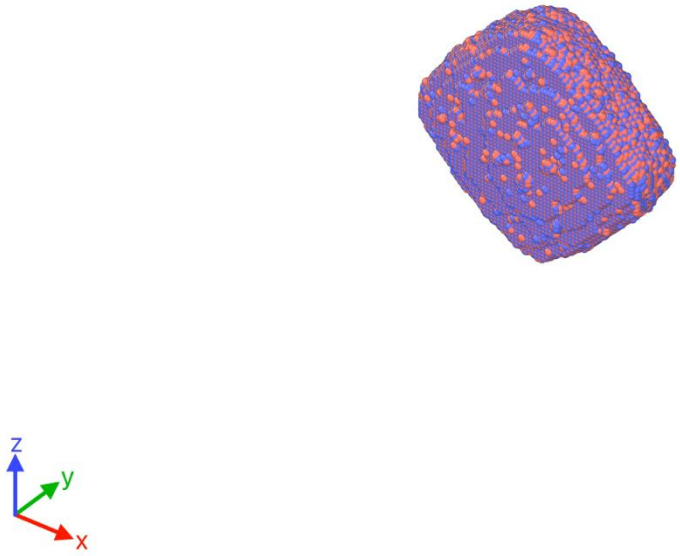


SVideo2. Surface evolution of TaB crystal during exposure to 2000 °C.

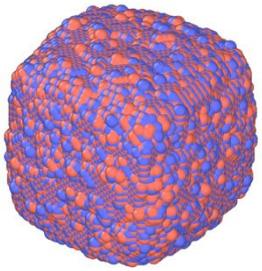


SVideo3. Surface evolution of ZrB crystal during exposure to 2000 °C.

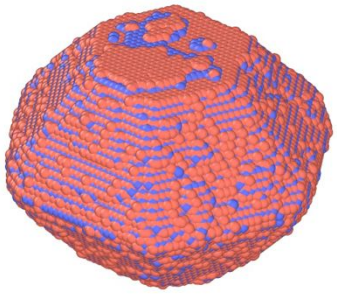

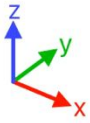


SVideo4. Surface evolution of $ZrB_2$ crystal during exposure to 2000 °C.

## References

[R1] Leone FC, Johnson NL. Statistics and Experimental Design In Engineering and the Physical Sciences. Vol 2. N.Y.: John Wiley and Sons; 1964.

[R2] Healy D. (2022). AnisoVis (https://github.com/DaveHealy-github/AnisoVis), GitHub. Retrieved May 26, 2022.

[R3] Jain A, Ong SP, Hautier G, Chen W, Richards WD, Dacek S, Cholia S, Gunter D, Skinner D, Ceder G, Persson KA. The Materials Project: A materials genome approach to accelerating materials innovation. APL Materials. 2013;1[1]:011002. https://doi.org/10.1063/1.4812323.

[R4] Berg S, Kutra D, Kroeger T. et al. ilastik: interactive machine learning for (bio)image analysis. Nat Methods 2019;16:1226–1232. https://doi.org/10.1038/s41592-019-0582-9.

[R5] Lawn BR, Fuller ER. Equilibrium penny-like cracks in indentation fracture. J Mater Sci. 1975;10:2016–2024. https://doi.org/10.1007/BF00557479.

[R6] Anstis GR, Chantikul P, Lawn BR, Marshall DB. A critical evaluation of indentation techniques for measuring fracture toughness: I, direct crack measurements. J Am Ceram Soc. 1981;64[9]:533–538. https://doi.org/10.1111/j.1151-2916.1981.tb10320.x.

[R7] Niihara K, Morena R, Hasselman DPH. Evaluation of KIc of Brittle Solids by the Indentation Method with Low Crack-to-Indent Ratios. J Mater Sci

Lett. 1982;1:13–16. https://doi.org/10.1007/BF00724706.

[R8] Stukowski A. Visualization and analysis of atomistic simulation data with OVITO–the Open Visualization Tool. Modelling Simul Mater Sci Eng. 2010;18:015012. https://doi.org/10.1088/0965-0393/18/1/015012.

[R9] Anderson MW, Gebbie-Rayet JT, Hill AR, et al. Predicting crystal growth via a unified kinetic three-dimensional partition model. Nature 2017;544:456–459. https://doi.org/10.1038/nature21684.

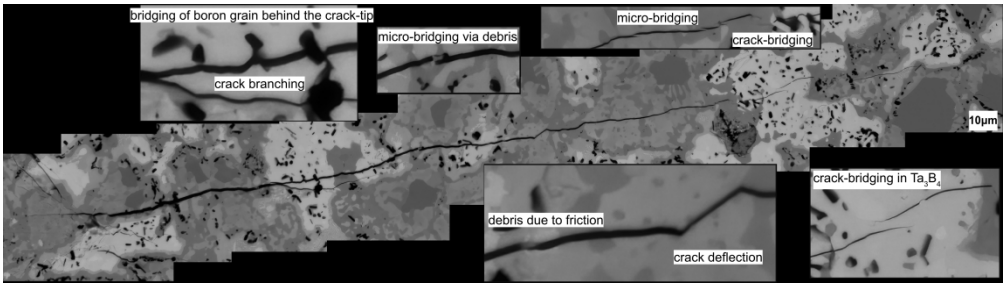


Representative crack propagation in the multiboride ceramic after the indentation test using a 196 N load